bioRxiv preprint doi: https://doi.org/10.1101/2024.02.25.581922; this version posted April 15, 2025. The copyright holder for this preprint (which was not certified by peer review) is the author/funder, who has granted bioRxiv a license to display the preprint in perpetuity. It is made available under aCC-BY-NC-ND 4.0 International license.

1 # Shallow-water chemosymbiotic clams are a globally significant and
2 # previously overlooked carbon sink

3

4 Menggong Li[1,2#], Yunlong Li[1,2#], Shi-Hai Mao[3#], Zhixin Zhang[4], Chong Chen[5], Xueying Nie[1,2],
5 Xu Liu[1,2], Hui Wang[1,2], Xiaoshou Liu[1], Weipeng Zhang[1], Qiang Lin[4], Guang-Chao Zhuang[3]*,
6 Jin Sun[1,2]*

7 **Affiliations:**

8 [1] Key Laboratory of Evolution & Marine Biodiversity (Ministry of Education) and
9 Institute of Evolution & Marine Biodiversity, Ocean University of China, Qingdao
10 266003, China

11 [2] Laboratory for Marine Biology and Biotechnology, Qingdao Marine Science and
12 Technology Center, Laoshan Laboratory, Qingdao 266237, China

13 [3] Frontiers Science Center for Deep Ocean Multispheres and Earth System, and Key
14 Laboratory of Marine Chemistry Theory and Technology, Ministry of Education, Ocean
15 University of China, Qingdao, 266100, China

16 [4] CAS Key Laboratory of Tropical Marine Bio-resources and Ecology, South China Sea
17 Institute of Oceanology, Chinese Academy of Sciences, Guangzhou, China

18 [5] X-STAR, Japan Agency for Marine-Earth Science and Technology (JAMSTEC), 2-15
19 Natsushima-cho, Yokosuka, Kanagawa Prefecture 237-0061, Japan

20 [#] equal contribution

21 * Corresponding authors: Jin Sun (jin_sun@ouc.edu.cn) or Guang-Chao Zhuang
22 (zgc@ouc.edu.cn)

bioRxiv preprint doi: https://doi.org/10.1101/2024.02.25.581922; this version posted April 15, 2025. The copyright holder for this preprint (which was not certified by peer review) is the author/funder, who has granted bioRxiv a license to display the preprint in perpetuity. It is made available under aCC-BY-NC-ND 4.0 International license.

Abstract

Chemosynthetic animal symbioses are common in marine ecosystems but remain overlooked as contributors to global carbon fixation. We show that the shallow-water thyasirid clam *Thyasira tokunagai*, dominant in Yellow Sea sediments, harbors sulfur-oxidizing *Sedimenticola* symbionts with remarkably consistent genomic contents and functionality across the region, showing active Calvin cycle gene expression and close-knit host-symbiont metabolic integration. Field surveys demonstrated densities up to 2015 individuals·m^{-2}, while radiocarbon tracing revealed assimilation rate constants (0.002–0.005 day^{-1}) peaking at 14.8°C. Spatial modelling combining abundance and temperature estimated a carbon fixation of 0.89 Tg C·yr^{-1} in Yellow Sea, equivalent to 43% of the annual sedimental C burial from the Chinese coast. The species complex that includes *T. tokunagai* is widely distributed and constitutes a globally significant, previously unaccounted blue carbon sink. Our findings underscore the crucial role of shallow-water chemosymbioses in carbon cycling, emphasising the importance of incorporating them into climate models and conservation strategies focused on carbon sequestration.

INTRODUCTION

Carbon fixation is a fundamental process converting inorganic carbon into organic compounds and underpins the entire global food web (*1*). Photosynthesis, a light-driven process, accounts for the majority of primary productivity on Earth. Chemosynthesis, best known from deep-sea environments, represents the more ancient form of primary production. Chemoautotrophic microorganisms obtain the chemical energy to fix inorganic carbon through the oxidation of reducing substances, such as sulfides, methane, and hydrogen gas, providing an alternative carbon fixation pathway to photosynthesis (*2*). Increasing evidence indicates that chemosynthesis supports diverse microbial and animal life across the entire ocean, influencing the global biogeochemical cycling of nutrients and the marine carbon budget (*2-4*).

Chemosynthetic microorganisms are widely distributed throughout marine ecosystems, inhabiting all depth zones and latitudinal gradients (*2*). Most studies on dark carbon fixation in marine ecosystems focus on free-living chemoautotrophic bacteria. Significant dark carbon fixation also occurs in coastal sediments, where maximum chemoautotrophy rates reach 3-36 mmol C·m^{-2}·d^{-1} in the upper 1-2 cm (*5*). In the deep ocean, benthic dark inorganic carbon fixation (DCF) rates ranges between $1.51*10^{1}$-$3.24*10^{2}$ μg C·m^{-3}·h^{-1} in the water column and $1.15*10^{4}$-$1.83*10^{5}$ μg C·m^{-3}·h^{-1} in sediments (*3*). In contrast to free-living chemoautotrophic bacteria, chemosymbiotic animals house chemosynthetic microbes in specific organs or cells, functioning as ‘ecological containers’ (*6*). This intimate partnership is exemplified by symbiotic tubeworms, bivalves, and gastropods inhabiting deep-sea vent and seep ecosystems (*6-8*). Chemosymbiosis also extends to shallow-water environments, however, encompassing ciliated protists, nematodes, gutless oligochaetes, and lucinid clams associated with seagrass or mangrove sediments, as well as thyasirid bivalves inhabiting organic-rich, cold-water

bioRxiv preprint doi: https://doi.org/10.1101/2024.02.25.581922; this version posted April 15, 2025. The copyright holder for this preprint (which was not certified by peer review) is the author/funder, who has granted bioRxiv a license to display the preprint in perpetuity. It is made available under aCC-BY-NC-ND 4.0 International license.

64 sediments (*8*). Biological carbon fixation exerts a notable influence on global carbon budgets
65 (*9*). Despite the recognized importance of chemosymbiosis, the contribution of shallow-water
66 chemosynthetic symbioses to regional or global carbon budgets remains unquantified. So far,
67 only one study estimated the carbon and nitrogen fate in shallow-water lucinid clams, using
68 stable isotope incubation – with an estimated carbon fixation rate of 300-2600 nmol C·g gill
69 tissue^{-1}·h^{-1} – but less is known about the carbon fixation budget (*10*).
70
71 Here, we use a thyasirid clam prevalent in the reducing sediments in the Yellow Sea –
72 *Thyasira tokunagai* (**Fig. 1A)** – as a model for quantifying the carbon fixation contribution of
73 chemosymbiotic animals in shallow water. *Thyasira tokunagai* is a member of the widely
74 distributed *T. gouldii* species complex commonly found in reducing sediments all around cold
75 shallow-water habitats around the northern hemisphere from eastern Canada to Europe to
76 Asia (*11-13*). Quantifying the carbon fixation contribution of the *T. tokunagai* is crucial for a
77 more complete understanding of carbon cycling in the Yellow Sea and other similar coastal
78 ecosystems (*14*), which provides an opportunity to address this gap. Our findings highlight
79 chemosymbiotic animals as a previously unappreciated carbon sink in shallow water,
80 comparable to well-known carbon sequestration ecosystems such as mangroves and seagrass
81 beds.
82
83 **RESULTS**
84 **Host-Symbiont System in a Homogeneous, Shallow Environment**
85 Our sampling records across seven cruises between 2018 to 2024 show that *Thyasira*
86 *tokunagai* is a dominant benthic species in the Yellow Sea, with up to 2015 individuals per
87 square meter, typically found at depths ranging from 9-82 meters **(table S1)**. *Thyasira*
88 *tokunagai* was identified from both morphology and the mitochondrial *cox1* gene barcode to
89 confirm its placement in the *Thyasira gouldii* species complex (**Fig. 1A and fig. S1A**;
90 personal communications, Suzanne Dufour). Pairwise comparisons of the *cox1* gene of
91 specimens collected from nine sampling locations in the Yellow Sea revealed an average of
92 99.84% similarity (**fig. S1B**), and the haplotype network (**fig. S1C**) also showed that nearly
93 all haplotypes lacked a clear geographical affinity. Furthermore, our STRUCTURE analysis
94 also showed a lack of population differentiations using the alignment of 13 protein-coding
95 genes (PCGs) of 30 mitochondrial genomes based on the delta K (K = 2; **fig. S1D**). These
96 results indicate a panmixia condition for all nine populations of *T. tokunagai* sampled in the
97 Yellow Sea.
98
99 Compared to other benthic fauna and environmental samples from the Yellow Sea (*15*), *T.*
100 *tokunagai* exhibited the lowest δ^{15}N value (-0.23 ± 0.22 ‰, n = 3), suggesting a potential
101 autotrophic supplement on its nitrogen source (**Fig. 1B and table S2**; particulate organic
102 matter (POM): 2.08 ‰, phytoplankton: 6.28 ‰, benthic fauna: 10.77 ‰). The δ^{13}C value of *T.*
103 *tokunagai* (-20.52 ± 0.43 ‰, n = 3) was higher than that of the POM and phytoplankton, but
104 lower than other benthic fauna (POM: -24.87 ‰, phytoplankton: -24.35 ‰, benthic fauna:
105 -17.46 ‰). These results indicate that *T. tokunagai* does not rely on the filtration or predation
106 of other organisms for nutrition, though it may obtain organic matter from others.

bioRxiv preprint doi: https://doi.org/10.1101/2024.02.25.581922; this version posted April 15, 2025. The copyright holder for this preprint (which was not certified by peer review) is the author/funder, who has granted bioRxiv a license to display the preprint in perpetuity. It is made available under aCC-BY-NC-ND 4.0 International license.

107
108 A bacterial species belonging to the genus *Sedimenticola* dominated the bacterial community
109 in the gills of *T. tokunagai* (**fig. S2**), determined through full-length 16S rRNA gene amplicon
110 sequencing, showing this *Sedimenticola* species accounted for an average of 92.34% of the
111 bacterial community (n = 21). Phylogenetic reconstruction using the 16S rRNA gene
112 confirmed that its closest relative was the chemosymbiont of *T.* cf. *gouldii* in the same species
113 complex (**fig. S3**). To investigate the distribution of symbionts within the gill tissue, we
114 conducted fluorescent *in situ* hybridization (FISH) imaging, which show that 1) the
115 symbionts were concentrated in the bacteriocytes located at the middle part of the gill
116 filament except the ciliated filament tip (**Fig. 1C and fig. S4**) and 2) symbionts seemed to be
117 enveloped by a layer of membrane (indicated by the green signal). Nonetheless, transmission
118 electron microscopy (TEM) observation (**Fig. 1D**) of the gill tissue showed that symbionts
119 were actually localized in extracellular pouch-like structures among the microvilli but not
120 completely enclosed in vesicles, implying an exocellular symbiotic mode where bacteria are
121 maintained outside of the host cytoplasm but in a specialized pouch-like organ (*16*).
122

123 **Two Symbiont Phylotypes**

124 Two phylotypes of the same *Sedimenticola* species made up the bacterial population in *T.*
125 *tokunagai*. There was only a single base pair difference (G vs A) between these two
126 phylotypes at the 590rd position of the 16S rDNA, verified by Sanger sequencing
127 (**Supplementary Note 1**) – each phylotype accounting for 46.29% and 45.88% of the overall
128 symbiont population (mean percentage), respectively (**Fig. 2A**). Host individuals differ
129 greatly in the proportion of the two phylotypes, showing a whole range including some with
130 only one or the other phylotype (**Fig. 2B**). Spot-analyses (10 µm in diameter) of gills showed
131 that over 80.59% of 10,468 spots exhibited just one phylotype, indicating there is a bias to
132 hosting just one phylotypes within each symbiotic pouch. H&E imaging and FISH analysis
133 confirmed the symbiont distribution pattern on the gill filament (**Fig. 2, C and D**). Spatial
134 analyses of gills show that individuals also vary in the level of spatial heterogeneity
135 concerning the phylotypes (two gills per individual, **Fig. 2E**) – especially in the individual g5
136 (a total of six individuals), which showed well-mixed patterns of the two phylotypes.
137
138 Combining long-read and short-read sequencing, a total of 30 high-quality circular genomes
139 (i.e. MAGs) were assembled, with completeness > 99.23%, contamination rate < 0.34%, and
140 size of 4.5 Mb **(Fig. 3A and table S3**). The average nucleotide identity (ANI) of these 30
141 MAGs ranges from 98.90 to 99.94% (**fig. S5 and table S4)**, above the proposed threshold of
142 inter-species variation of prokaryotes (95%) and supports them as belonging to the same
143 species (*17*). Representative genome of each phylotype was further deduced using
144 StrainPanDA **(Fig. 3A)**. Genome capacity analysis revealed no functional gene differences
145 between the two phylotypes **(table S5).** To boost the credibility of our findings, we conducted
146 a correlation analysis. This analysis revealed a positive correlation between the percentage of
147 phylotype G from StrainPanDA and the percentage of metagenomic reads of G base pair at
148 the 563rd position in 16S rRNA gene (**fig. S6; R^2 = 0.97, P < 0.001**). Their placement in the

bioRxiv preprint doi: https://doi.org/10.1101/2024.02.25.581922; this version posted April 15, 2025. The copyright holder for this preprint (which was not certified by peer review) is the author/funder, who has granted bioRxiv a license to display the preprint in perpetuity. It is made available under aCC-BY-NC-ND 4.0 International license.

149 genus *Sedimenticola* was also shown by phylogenetic reconstruction at the genomic level
150 **(Fig. 3B)**. Overall, it seems the two phylotypes are equivalent in function and the host
151 individuals do not actively select for one or the other phylotype, instead using them
152 interchangeably.
153

154 **Symbiont Chemosynthetic Capacity Ensures Carbon Fixation**

155 The metabolic potential of the *Sedimenticola* symbiont of *T. tokunagai* was highly conserved
156 (**Fig. 4A**), highly similar to the published result in the closely related *T.* cf. *gouldii* (*18*). They
157 encode the full set of enzymes in carbon fixation and utilization, including the
158 Calvin–Benson–Bassham cycle (CBB cycle, or the reductive pentose phosphate cycle),
159 glycolysis/gluconeogenesis, tricarboxylic acid cycle (TCA), and oxidative phosphorylation,
160 enabling both phylotypes to assimilate dissolved inorganic carbon. The ribulose-bisphosphate
161 carboxylase large chain (*rbcL*, K01601) in the Calvin cycle is responsible for the assimilation
162 of inorganic carbon. The reductive TCA cycle cannot function completely in *T. tokunagai*
163 symbiont due to the absence of type II ATP citrate lyase, unlike the symbiont of the giant
164 tubeworm *Riftia pachyptila* (*19*). The complete dissimilatory nitrate reduction pathway
165 proceeds with respiration under an anaerobic or hypoxic environment but hinders it from
166 producing ammonia due to the lack of the nitrite reductase (NADH) large subunit (K00362).
167 A complete dissimilatory sulfate reduction pathway and a partial SOX system were also
168 found, mainly containing *soxA*, *B*, *X*, *Y*, and, *Z*, but *soxCD* was lacking. The incomplete
169 assimilatory sulfate reduction pathway was detected, which contained *sat* and *cysC*. We also
170 found the genes and enzymes related to hydrogen oxidation, containing *hoxF*, *U*, *Y*, *H*, *hybC*,
171 and *hyaB*. The symbiont encodes ABC transporters and PTS pathways, indicating the
172 capacity of heterotrophy. The bacterial chemotaxis and flagellar assembly pathways were
173 found. Additionally, both phylotypes have a relatively complete capacity for the biosynthesis
174 capacity of amino acids (17), vitamins, and cofactors (10) **(table S6)**, suggesting a capacity
175 for free-living habit. The genes in the pathways that are highly relevant to chemosynthesis are
176 expressed actively, such as the CBB cycle, sulfur oxidation, and nitrogen metabolism (**Fig.
177 4B**).

178

179 **Carbon fixation flux estimation**

180 Since the *Thyasira gouldii* complex is widely distributed and abundant across shallow
181 cold-water habitats of the northern hemisphere, with potential to be a carbon sink, we
182 proceeded to estimate the carbon fixation flux and carbon sequestration capacity of *T.
183 tokunagai* as a model (**Fig. 5A**). The enzyme activity in animals alters with temperature. To
184 assess the carbon assimilation activity of clams, we added ^{14}C-labeled DIC tracers to
185 homogenized bacterial solution from the same sampling site (four sites in total in this study,
186 **Fig. 5B**). Considering the impact of varying symbiont numbers, we chose four replicate
187 samples from each site. All samples for each site were incubated at four temperatures (i.e., 5,
188 12, 20, and 28 °C), covering the lowest and highest levels across a whole year in the natural

bioRxiv preprint doi: https://doi.org/10.1101/2024.02.25.581922; this version posted April 15, 2025. The copyright holder for this preprint (which was not certified by peer review) is the author/funder, who has granted bioRxiv a license to display the preprint in perpetuity. It is made available under aCC-BY-NC-ND 4.0 International license.

189 habitat (**Fig. 5C and table S7**). Results showed that the carbon assimilation rate constant (*k*)
190 was lowest at 5 °C across all sites (average: 0.002148 ± 0.001372). As temperature
191 increased, the *k* exhibited higher levels, with the highest and comparable values at 12 and
192 20 °C (0.005092 ± 0.000448 and 0.004788 ± 0.000976, respectively). A declining trend was
193 observed with the continuously rising temperature until 28 °C (*k* = 0.003508 ± 0.001204),
194 only accounting for 69% of the highest *k* value. The Wilcoxon Signed-Rank test (**fig. S7**)
195 indicated significant differences at the same temperature, but only between some sites,
196 suggesting that symbiont copy number and metabolic activity may influence carbon
197 assimilation activity. Nonetheless, symbionts in *T. tokunagai* appear to transfer more DIC to
198 organic matters at elevated temperature. A cubic regression model presented a better
199 performance in regression from measured value, than a quadratic one (**Fig. 5C and fig. S8**),
200 predicting a peak assimilation rate constant at 14.78 °C, with decreasing under both warmer
201 and cooler conditions.
202
203 Previous cruises and research reported that the dissolved inorganic carbon (DIC) in the
204 bottom water fluctuated within a small range between 2.03 and 2.23 mmol/L (*20*).
205 Furthermore, we applied kriging interpolation to estimate the annual average bottom-water
206 temperature (average level in year) and the spatial distribution of *T. tokunagai* across the
207 Yellow Sea (**Fig. 6, A and B**). The results showed that annual bottom-water temperature
208 ranged from 6 to 16 , and three major inhabiting groups aggregated in the active cold-water
209 mass regions (**Fig. 6, A and B**). Based on the established relationship between temperature
210 and the carbon assimilation rate constant (**Fig. 5C**; $R^2 = 0.52$, $P = 1.02e^{-07}$), we estimated the
211 spatially resolved carbon fixation rate of *T. tokunagai* symbionts in the Yellow Sea (**Fig. 6C**).
212 The cold-water mass of northern region in Yellow Sea was the central contributor in carbon
213 assimilation, with a peak fixation rate of 27.1791 $g \cdot m^{-2} \cdot yr^{-1}$, coinciding with areas of high *T.*
214 *tokunagai* abundance. Considering the areal extent of the Yellow Sea, we estimated that the
215 total annual carbon fixation rate by *T. tokunagai* symbionts in the region was approximately
216 0.892 $Tg \cdot C \cdot yr^{-1}$.
217

218 **DISCUSSION**

219 **Chemosynthetic capacity of thyasirids in the Yellow Sea**

220 Chemosymbiosis is widely distributed in Mollusca, but most studies have been undertaken in
221 deep-sea vents and seeps (*6, 7*). Most members of the family Thyasiridae are widely
222 distributed in non-vent/seep anoxic mud, including shallow-water ecosystems, but they
223 remain little-studied and their role in ecosystems much overlooked. Our results are the first
224 detailed study on the symbiosis of *Thyasira tokunagai* despite its abundance, revealing the
225 dominance of a sulfur-oxidizing bacterial (SOB) symbiont belonging to *Sedimenticola* in
226 their gills clustering closely with other previously reported chemosymbionts of other animals
227 (**fig. S2**).
228
229 Consistent with previous metagenomic work on the closely related congener *T.* cf. *gouldii*
230 (*18*), the *T. tokunagai* symbiont genomes also exhibited *soxA, B, X, Y,* and *Z*, but not *soxCD*.
231 The absence of *soxCD* would lead to the partial oxidation of thiosulfate and the accumulation

bioRxiv preprint doi: https://doi.org/10.1101/2024.02.25.581922; this version posted April 15, 2025. The copyright holder for this preprint (which was not certified by peer review) is the author/funder, who has granted bioRxiv a license to display the preprint in perpetuity. It is made available under aCC-BY-NC-ND 4.0 International license.

232 of zero-valent sulfide, forming sulfur globules in the symbionts, which are common in SOB
233 such as *Erythrobacter flavus* (*21*) and *Chlorobaculum limnaeum (22)*. Sulfur globule-like
234 structures were observed in the symbiont of both *T. flexuosa* and *T.* cf. *gouldii* under TEM
235 (*23, 24*). On the other hand, genomes of our *T. tokunagai* symbiont contained a complete
236 dissimilatory sulfate reduction (*dsr*) pathway, suggesting the genetic basis to fully oxidize
237 sulfide to sulfate (*25*). During that process, ATP is generated by sulfate adenylyltransferase
238 (*sat*) and then utilized in the Calvin cycle to fix CO_2, which is a central principle of
239 chemosymbiosis. Additionally, *T. tokunagai* symbionts appear to be capable of fixing
240 inorganic carbon via oxidizing reducing substances, with the SOX system, reverse
241 dissimilatory sulfate reduction pathway, and the HOX system (*26, 27*). The capability of
242 dissolved inorganic carbon assimilation has been quantified, providing robust support of
243 hosting chemosymbiont in *T. tokunagai.*
244
245 **Strong selection of host on symbiont and horizontal transmission**
246 Though our sampling sites of *T. tokunagai* covered a wide area in the Yellow Sea, with the
247 longest distance from the southernmost point to the northernmost point over 500 km, there
248 was an undifferentiated population panmictic across all sites as evidenced by mitochondrial
249 population genomics. The presence of the symbiont population in the gill of *T. tokunagai* is
250 greatly dominated by a single symbiont species (genus *Sedimenticola*) points to the strong
251 selection of symbionts by the host (*28*). The ratio of the two phylotypes within each host
252 likely result from local bias within each symbiont-hosting pouch (spatial metabarcoding
253 result in **Fig. 2E**). Overall, we observed a lack of bias in phylotype uptake by the host, with a
254 comparable percentage of the two phylotypes across the whole *T. tokunagai* populations and
255 a spatial section consisting of the mixed pattern. The two phylotypes differ only by one single
256 base pair in the 16S rRNA gene and appear to be without functional differentiation, supported
257 by the highly similar gene sets between the two deduced phylotypes' genomes. This is
258 different from the symbiont phylotypes diversity in deep-sea bathymodioline mussels, which
259 has a significant impact on the fitness (*29*). Our results suggest all individuals of *T. tokunagai*
260 share symbionts of a consistent function and ecology – enabling a reliable extrapolation of
261 our measured carbon fixation rate to the whole Yellow Sea population.
262
263 Previous studies reported the super extensile foot in thyasirid bivalves to mine sulfide and the
264 magnetosome in its symbionts (*30, 31*), implying the symbionts might be derived from the
265 specific niche of sediments. The metabolic potential of the symbiont genomes, with the
266 capacity for heterotrophy and free-living, is suggestive of horizontal transmission. Therefore,
267 we consider *T. tokunagai* most likely acquire the *Sedimenticola* symbionts from the
268 environment via horizontal transmission, acquired under the control of a highly selective
269 mechanism.
270
271 **An overlooked sink of carbon dioxide from chemosynthetic thyasirids in shallow water**
272 Global climate change, primarily driven by anthropogenic activities, is occurring at an
273 unprecedented pace compared to past climatic fluctuations (*32, 33*). Achieving net-zero CO_2
274 emissions is critical to mitigating this trend, necessitating accurate quantification of carbon

bioRxiv preprint doi: https://doi.org/10.1101/2024.02.25.581922; this version posted April 15, 2025. The copyright holder for this preprint (which was not certified by peer review) is the author/funder, who has granted bioRxiv a license to display the preprint in perpetuity. It is made available under aCC-BY-NC-ND 4.0 International license.

275 sinks, particularly blue carbon, i.e., carbon captured by marine ecosystems. Previous research
276 has largely focused on conventional blue carbon contributors such as phytoplankton, marine
277 microbes, mangroves, and seagrasses (*9, 34*). However, holobiont animals that fix carbon
278 through chemosynthesis primarily using the CBB cycle with minor contribution from the
279 rTCA cycle may represent an underestimated and significant carbon sink. Compared to
280 charismatic species such as the giant tubeworm *Riftia pachyptila* that only live-in biodiversity
281 hotspots like vents, chemosymbiotic bivalves in families like Thyasiridae and Lucinidae in
282 anoxic shallow-water habitats are distributed across vast geographic ranges and should
283 represent a much higher total carbon flux. Despite this, few studies have explored the rate of
284 carbon assimilation in chemosynthetic holobionts and their potential importance for oceanic
285 carbon fixation.
286
287 Here, we combine genomic and transcriptomic analyses and reveal the molecular
288 mechanisms underlying carbon fixation in the chemosymbionts of *Thyasira tokunagai*. Using
289 radiocarbon tracing technique, we also quantified its carbon fixation rate. Our results revealed
290 that each *T. tokunagai* individual can fix up to 34.3–37.9 mg C·yr^{-1}, with rates mainly
291 affected by symbiont density and the ambient temperature. Nevertheless, based on the
292 population density of *T. tokunagai*, we approximated an aerial carbon fixation rate of up to
293 27.2 g C m^{-2} yr^{-1} based on our rate measurement. Importantly, our multi-omics analyses show
294 that the symbiont populations of *T. tokunagai* across the entire Yellow Sea is remarkably
295 consistent in genomic content with only two phylotypes that share the same functionality;
296 meaning our estimated rate can be reliably applied to all individuals of *T. tokunagai*. This
297 value is significantly higher than the carbon fixation rates reported for many shallow-water
298 and terrestrial ecosystems, as well as deep-sea dark DIC fixation rates, such as lake sediment,
299 seawater, and soil (*35, 36*). Although the rate is lower than those of mangroves (170-190 g
300 C·m^{-2}·yr^{-1}) and seagrass (5-379 g C·m^{-2}·yr^{-1}), the broad distribution and high abundance of *T.*
301 *tokunagai* in the Yellow Sea compensates it in scale, yielding an estimated total carbon
302 fixation of 0.892 Tg C·yr^{-1}. This value is comparable to 43% of the total carbon burial rates
303 along the Chinese coast (up to 2.06 Tg C·yr^{-1}), which consisted of 0.05 Tg C·yr^{-1} from
304 mangrove (25,900 ha), 0.50 Tg C·yr^{-1} from salt marsh (297,900 ha), and 0.28-1.5 Tg C·yr^{-1}
305 from tidal flat (237,450-1,102,400 ha) (*34*). If counted based on the capability of mangrove
306 (~ 180 g C·m^{-2}·yr^{-1} averagely), the contribution from *T. tokunagai* in the Yellow Sea is
307 equivalent to about 495,000 ha mangrove and 2% of global mangrove (*34*). Furthermore,
308 thyasirids burrow deep in the anoxic mud and may tend to reserve the fixed carbon in the
309 sediment, based on moderated turbulence at the sediment-water interface compared to the
310 more dramatic waves in the intertidal region where mangroves and seagrasses are located.
311
312 The *Thyasira gouldii* complex, which *T. tokunagai* is a part of, is widely distributed across
313 the cold-water region across the entire northern hemisphere (**Fig. 5A**). Like the symbionts of
314 *T. tokunagai*, those of *Thyasira* cf. *gouldii* have a complete Calvin–Benson–Bassham (CBB)
315 cycle, indicating a high carbon fixation potential for the *Thyasira gouldii* complex (*18*). We
316 found a temperature dependence of carbon assimilation in chemosymbiotic thyasirids, while
317 the typical bottom-water temperature in Yellow Sea where the majority of *T. tokunagai*

bioRxiv preprint doi: https://doi.org/10.1101/2024.02.25.581922; this version posted April 15, 2025. The copyright holder for this preprint (which was not certified by peer review) is the author/funder, who has granted bioRxiv a license to display the preprint in perpetuity. It is made available under aCC-BY-NC-ND 4.0 International license.

318 inhabits is between 6-10 °C, within the climbing curve of the rate constant-temperature
319 relationship (**Fig. 5C**). Recently, marine heatwaves have been increasingly observed in the
320 deeper layers, persisting for longer and more intense than the surface seawater (*37*). For
321 instance, bottom water temperatures at depths of 50–100 m along the North American
322 continental shelf increased by up to 3 °C between 1993 and 2019, with similar phenomenon
323 observed in the deep water of high latitude regions (*38, 39*). Previous projections had
324 indicated an increase of 0.5 °C in the cold water mass by the end of 2050 (*40*), which could
325 enhance carbon fixation by 4.37% by the chemosymbionts of *T. tokunagai* by the end of 2050,
326 if the survival and distribution of *T. tokunagai* are not significantly affected by this (**fig. S9A**).
327 Likewise, a further increase of 2 °C by 2100 could increase carbon fixation by up to 17.71%
328 (**fig. S9B**). These predictions highlight the potential increase of carbon fixation by
329 shallow-water chemosymbiotic communities in a climate change scenario.
330
331 Collectively, our study used multi-omics and radiotracer techniques to elucidate the carbon
332 fixation potential of shallow-water thyasirid holobionts. Our findings reveal a previously
333 unrecognized carbon sink and highlight the ecological importance of shallow-water
334 chemosynthetic symbioses in marine carbon cycling. Considering that *T. gouldii* complex
335 (including *T. tokunagai*) is a dominant species in the Yellow Sea, Japan Sea, as well as the
336 pan-Arctic area in Atlantic and Pacific Ocean (*11, 12*), the *T. gouldii* complex or other
337 chemosymbiotic species may play a more substantial role in marine DIC fixation than
338 previously recognized. Further ecological investigation into the distribution and density of
339 these chemosymbiotic organisms, along with in-depth studies of the factors influencing their
340 carbon fixation rate, is crucial to accurately assess their contribution to global carbon cycling.
341

342 MATERIALS AND METHODS

343 Sampling description

344 *Thyasira tokunagai* (**Fig. 1A**) were collected from a total of 139 sites in the Yellow Sea
345 between 42-72 m depth from seven cruises on-board the R/V *Lanhai 101* from 2018 to 2024,
346 with the site details and environmental parameters shown in **table S1**. A 0.1 m^2 box corer was
347 employed to collect the surface sediments. The *T. tokunagai* were manually picked out from
348 the sediments via a 0.5 mm sieve once they were on board and then immediately fixed and
349 preserved. For details on the sample preservation, please see the supplementary information.
350

351 Stable isotope analysis

352 Stable isotope analysis of carbon (C) and nitrogen (N) was conducted as previously described
353 (*41*). The whole tissues of three *T. tokunagai* specimens were freeze-dried for two hours at
354 -60 , and approximately 0.1 mg of the powdered sample was analyzed for stable isotopes
355 using an isotope ratio mass spectrometer (IRMS, Sercon Instruments, Crewe, UK) at the
356 Third Institute of Oceanography, China. The carbon isotope abundance ratio was calculated
357 using the international standard VPDB (Vienna Peedee Belemnite) to determine the $\delta^{13}C$
358 value, with an analytical precision of ±0.2‰. Similarly, the nitrogen isotope abundance ratio
359 was based on atmospheric nitrogen to calculate the $\delta^{15}N$ value, with an analytical precision of

bioRxiv preprint doi: https://doi.org/10.1101/2024.02.25.581922; this version posted April 15, 2025. The copyright holder for this preprint (which was not certified by peer review) is the author/funder, who has granted bioRxiv a license to display the preprint in perpetuity. It is made available under aCC-BY-NC-ND 4.0 International license.

±0.25‰. Additional data on other macrobenthos in the Yellow Sea can be found in **Table S2** (*15*).

Transmission electron microscopy

Gill tissues were fixed overnight using a solution containing 2.5% glutaraldehyde and 2% paraformaldehyde (PFA) in phosphate buffer (PBS). The tissue was washed in 0.1M PBS three times for 15 minutes each and then fixed with 1% osmium tetroxide (OsO4) for 1 hour, followed by additional wash using PBS. It was dehydrated through a methanol series (50%, 70%, 90%, and 100%, three times for 15 minutes each) and embedded in Epon 812 resin. Ultrathin sections (70 nm) were sliced using a Reichert ULTRACUT slicer (Austria) and stained with uranyl acetate and lead citrate double staining method (*42*) for 15 minutes each. Images were captured by a JEM 1200-EX (Japan) transmission electron microscopy (TEM) at an accelerating voltage of 80 kV.

Fluorescence *in situ* hybridization (FISH) and histology

For FISH experiments, the symbiont-specific probe with Cy5-labeled (5'-TCCTCTATCACACTCTAGCTCAGCAGTATC-3'), sense probe with CY3-labeled (5'-GATACTGCTGAGCTAGAGTGTGATAGAGGA-3'), and bacterial universal probe EUB338 with CY5-labeled were designed based on the corresponding representative 16S rRNA gene (*43*). Primer-BLAST was used to evaluate the specificity of the designed probes, with reference of the NCBI non-redundant nucleotide sequence database (*44*). Gill tissues (fixed in PFA and preserved in pure methanol) were dehydrated in 100% methanol for 30 minutes each, embedded in paraffin, and then sectioned into 7 µm thick slices using a semiautomatic microtome (Leica, Germany). After removing paraffin with xylene and ethanol, the sections were rehydrated in a decreasing ethanol series (100%, 95%, 80%, and 70%) for 15 minutes each, followed by hybridization at 46°C with a hybridization buffer (work concentration: 5 µg/mL probe in 0.9 M NaCl, 0.02 M Tris-HCl, 0.01% sodium dodecyl sulfate and 30% Formamide) for 1 h. Following hybridization, the slides were washed in a washing buffer (0.1 M NaCl, 0.02 M Tris-HCl, 0.01% sodium dodecyl sulfate, and 5 mM EDTA) at 48°C for 5 minutes each, and subsequently, the cell nucleus and cell membrane were stained with 4′,6-diamidino-2-phenylindole (DAPI, Solabio) and Alexa Fluor 488 Conjugate Concanavalin-A (Invitrogen, CA, USA) for 10 minutes at room temperature, respectively. After washing using PBST (Tween-20: PBS=1: 1000), the slides were mounted with ProLong Diamond Antifade Mountant (Invitrogen). Images were captured using a ZEISS LSM900 or Andor Dragonfly 302 confocal laser scanning microscope. For hematoxylin and eosin (HE) staining, dewaxed tissue sections were stained according to standard protocols. Subsequently, sections were dehydrated and mounted with neutral balsam. Images were captured by a pathological section scanner (Leica SDPTOP HS6)

Full-length amplicon sequencing

Genomic DNA was extracted from the whole or partial gill tissues (The whole gill divided into six parts) using the DNeasy Blood & Tissue Kit (Qiagen, Hilden, Germany), following the manufacturer's protocol. Meanwhile, DNA was also extracted from approximately 0.5 g

bioRxiv preprint doi: https://doi.org/10.1101/2024.02.25.581922; this version posted April 15, 2025. The copyright holder for this preprint (which was not certified by peer review) is the author/funder, who has granted bioRxiv a license to display the preprint in perpetuity. It is made available under aCC-BY-NC-ND 4.0 International license.

403 of ambient surface sediments (wet weight) by using the PowerSoil DNA Isolation Kit
404 (Qiagen, Hilden, Germany). NanoDrop Lite (Thermo Scientific, USA) and 1% agarose gel
405 electrophoresis were used to check the DNA quantity and quality, respectively. Full-length
406 16S rRNA gene of bacteria from sediments and *T. tokunagai* gill were also amplified by the
407 primers 27F and 1492R (*45*). High fidelity (HiFi) reads were generated from the PacBio RS
408 II platform by Novogene (Beijing, China) with CCS mode in gill samples and ambient
409 sediment samples, respectively. QIIME version 2023.9.1 (*46*) was used to data process with
410 the standard pipeline, containing quality control, Amplicon Sequence Variants (ASVs) /
411 phylotypes table construction, and taxonomic classification. ChiPlot
412 (https://www.chiplot.online) was used to visualize the relative abundance of the bacteria
413 community in the gill and sediment.
414
415 **Metagenome sequencing**
416 Genomic DNA intended for amplicon sequencing and the newly extracted DNA were both
417 employed for metagenomic sequencing. The newly extracted genomic DNA was obtained
418 from gill and whole tissue using the SDS method. The library was constructed by randomly
419 fragmenting the DNA into approximately 350 bp reads. Following library construction,
420 sequencing was conducted in paired-end 150 bp mode on an Illumina NovaSeq 6000
421 platform (Tianjin, China). Simultaneously, the long quality-checked DNA was sent to
422 Novogene (Tianjin, China) for library preparation and sequencing. For Oxford Nanopore
423 Technologies (ONT) sequencing, the library was generated using the SQK-LSK109 kit
424 (Oxford Nanopore Technologies, UK) in accordance with the manufacturer's guidelines.
425 Long raw reads were generated through basecalling with Guppy version 6.1.7 (*47*).
426
427 **Metatranscriptome sequencing**
428 Total RNA was extracted using TRIzol reagent (Invitrogen, CA, USA) with the guidance of
429 the manufacturer's protocol. RNA integrity and quantity were measured using the
430 Bioanalyzer 5400 system (Agilent Technologies, CA, USA). cDNA was obtained by
431 removing the prokaryotic and eukaryotic ribosomal RNA (rRNA of Animal, G-Bacteria, and
432 Plant) from the total RNA using the TIANSeq rRNA Depletion Kit for the construction of a
433 meta-transcriptomic library. The nucleic acid for metagenome and meta-transcriptome
434 sequencing was subjected to NovaSeq 6000 system (Illumina) at Novogene (Tianjin, China)
435 with paired-end mode and a read length of 150bp, and the ONT library was sequenced on the
436 PromethION platform at Novogene.
437
438 **Mitochondrial genome assembly and annotation**
439 Raw reads were trimmed to remove low-quality sequences and adapters using Trimmomatic
440 v.0.39 (*48*) with the following parameters: ILLUMINACLIP: TruSeq3-PE-2.fa:2:30:10,
441 LEADING:20, TRAILING:20, SLIDINGWINDOW:4:15, MINLEN:100. NOVOPlasty
442 v.4.3.1 (*49*) were employed to construct the mitochondrial genomes with default settings
443 (160M randomly selected reads per sample). Assembled mitochondrial genomes were
444 annotated on the MITOS web server (*50*) with the default setting except "the genetic code: 5
445 invertebrates".

bioRxiv preprint doi: https://doi.org/10.1101/2024.02.25.581922; this version posted April 15, 2025. The copyright holder for this preprint (which was not certified by peer review) is the author/funder, who has granted bioRxiv a license to display the preprint in perpetuity. It is made available under aCC-BY-NC-ND 4.0 International license.

446

447 **Host phylogenetic and population structure analysis**

448 A total of 24 *cox1* gene sequences in the family Thyasiridae were downloaded from the NCBI,
449 and three Lucinid sequences served as the outgroup in the phylogenetic analysis **(table S8)**.
450 Then, these sequences were aligned using MUSCLE v.5.1 (*51*), and the ambiguous alignment
451 was trimmed using Gblocks v.0.91b (*52*). The phylogenetic tree was constructed using the
452 Maximum Likelihood (ML) method in MEGA-X v.10.2.2 (*53*) and 100 bootstraps, and the
453 HKY + Γ model was suggested as the best model based on both AIC- and BIC-based
454 methods.

455 To understand the population differentiation of *T. tokunagai* in the Yellow Sea, the DnaSP v.6
456 (*54*) and PopART v.1.7 (*55*) with the median-joining Network method were employed to
457 investigate the haplotype network based on the alignment file. Furthermore, 13
458 protein-coding genes (PCGs) of 30 individuals were aligned separately using MAFFT v.7.515
459 (*56*) with the default parameter. Population structure analysis was performed based on the
460 mitochondrial genome by STRUCTURE v.2.3.4 (*57*) with the settings of "*K*: from 2 to 7,
461 2,000,000 iterations, and 10% of burnin". The most optimal *K* was determined using
462 Structure Harvester (*58*) web server with the delta *K* method.

463

464 **Symbiont genome assembly, binning, and annotation**

465 Short raw reads were trimmed using Trimmomatic version 0.39 (*48*) with the following
466 settings: TruSeq3-PE-2.fa:2:30:10:8:true SLIDINGWINDOW:5:20 LEADING:3
467 TRAILING:3 MINLEN:36. Clean reads were assembled using Megahit version 1.2.9 (*59*)
468 with default settings. The metagenome-assembled genomes (MAGs) were binned using
469 MaxBin version 2.2.7 (*60*), with the cutoff of contig length from 1000 to 2000 for the
470 optimization. To reduce the host contamination, we conducted a decontamination process
471 using BlobTools version 1.1.1 (*61*) with default settings, and then sequences belonging to the
472 phylum *Proteobacteria* were selected for downstream analyses. To obtain the circular-level
473 genome of the symbiont, firstly, the ONT long reads were mapped to the highest quality
474 MAGs; secondly, these long reads mapped were assembled using NextDenovo version 2.5.2
475 (*62, 63*); thirdly, clean reads from each sample (i.e. Illumina) were input into NextPolish
476 version 1.4.1 (*64*) to polish the circular-level genome. Then, these genomes were evaluated
477 for completeness and contamination using CheckM2 version 0.1.3 (*65*). GTDB-TK version
478 2.1.1 (*66*) was used to determine the taxonomy of symbionts at the genome level. The matrix
479 of pairwise average nucleotide identity (ANI) of 30 MAGs was generated using FastANI
480 version 1.34 (*17*). The Wilcoxon Rank-Sum test was employed to assess differences in ANI
481 values across symbiont phylotypes. 16S rRNA genes and open reading frames (ORFs) of
482 MAGs were predicted by Prokka version 1.14.6 (*67*) in the single genome mode. These
483 predicted genes of the pangenome were searched against the NR database using BLASTp in
484 DIAMOND version 2.0.15.153 (*68*) with an E-value cut-off of $1e^{-5}$. The results were further
485 used for Gene Ontology annotation by Blast2GO version 6.0 (*69*). Meanwhile, Clusters of
486 Orthologous Group 2020 (COG2020) (*70*) was adopted to classify the functional groups of
487 genes in the pangenome. The genes of the pangenome were annotated using BlastKOALA
488 (*71*) by searching against the KEGG database **(table S9)**.

bioRxiv preprint doi: https://doi.org/10.1101/2024.02.25.581922; this version posted April 15, 2025. The copyright holder for this preprint (which was not certified by peer review) is the author/funder, who has granted bioRxiv a license to display the preprint in perpetuity. It is made available under aCC-BY-NC-ND 4.0 International license.

489
490 **Spatial metabarcode sequencing**
491 We used the Stereo-seq FFPE pipeline (BGI, China) to investigate the spatial distribution
492 pattern between the two 16S phylotypes. The gills from six individuals were pre-fixed
493 overnight with 4% PFA and then embedded in paraffin. Three continuous sections from the
494 embedded block were cut at 10 μm thick. The second section was designated for chip loading
495 to capture rRNA, while the remaining two sections were used in staining (either HE or FISH).
496 The tissue section was adhered to the Stereo-seq chip (BGI, China) surface and incubated at
497 37□ for 3 minutes. The tissue sections were fixed in methanol and incubated at -20°C for 40
498 minutes prior to Stereo-seq library preparation. Where applicable, the same sections were
499 stained with a nucleic acid dye (Thermo Fisher, Q10212), and imaging was conducted using a
500 Stereo OR 100 microscopes in the FITC channel before *in situ* capture. After washing with
501 0.1X SSC buffer (Thermo, AM9770) supplemented with 0.05 U/ml RNase inhibitor (NEB,
502 M0314L), the tissue sections placed on the chip were permeabilized using 0.1% pepsin
503 (Sigma, P7000) in 0.01 M HCl buffer. They were incubated at 37°C for 5 minutes and
504 subsequently washed again with the same 0.1X SSC buffer with RNase inhibitor. cDNA was
505 synthesized on the chip using the FFPE MIX solution, consisting of 158 μL FFPE RT Buffer
506 mix, 30 μL FFPE RT Enzyme mix, 10 μL FFPE RT Oligo, and 2 μL FFPE Dimer, at 42°C for
507 5 hours. The cDNA-containing chips then underwent treatment with the Prepare cDNA
508 Release Mix (cDNA Release Enzyme and cDNA Release buffer) overnight at 55°C. The
509 harvested cDNA was purified using VAHTSTM DNA Clean Beads (0.8X) and subsequently
510 amplified in the amplification solution, which included 42 μL cDNA, 50 μL cDNA
511 amplification mix, and 8 μL FFPE cDNA Primer Mix. The PCR protocol was as follows:
512 initial denaturation at 95°C for 5 minutes, followed by 15 cycles of denaturation at 98°C for
513 20 seconds, annealing at 58°C for 20 seconds, and extension at 72°C for 3 minutes,
514 concluding with a final extension at 72°C for 5 minutes. After quantification using the Qubit
515 dsDNA HS kit, the cDNA product was utilized for library construction according to the
516 guidelines of the Stereo-seq 16 Barcode Library Kit V1.0. Raw reads were retrieved in
517 paired-end 75bp mode using MGI DNBSEQ-T7.
518
519 **Spatial metabarcode analyses**
520 Fastq files were generated from an MGI DNBSEQ-T7 sequencer. CID and MID are
521 contained in the read 1 (CID: 1-25 bp, MID: 26-35 bp), while the corresponding read 2
522 consists of the 16S rDNA sequences. The current SAW software version 8.0.2 (*72*) could not
523 differentiate the two 16S phylotypes with the difference of a single base pair. To visualize the
524 patterns, the pre-separation of reads containing the differentiated base pair fully matching to
525 the full length 16S rRNA gene were adopted. In detail, the normal analysis of Stereo-seq
526 reads were completed, with all the raw reads, ssDNA image, mask file, and reference. The
527 STAR genome reference was prepared with the *de novo* assembled transcriptional profile and
528 the 16S rRNA sequence (phylotype A). The produced *.bam* files were processed, with the
529 region (16S rRNA sequence: 907-953) kept. The A-phylotype reads were extracted if they
530 were uniquely mapped and completely matched to 16S rRNA (NH:i:1, MAPQ=255,
531 CIGAR=47M). Meanwhile, the G-phylotype reads were extracted as the same way, with the

bioRxiv preprint doi: https://doi.org/10.1101/2024.02.25.581922; this version posted April 15, 2025. The copyright holder for this preprint (which was not certified by peer review) is the author/funder, who has granted bioRxiv a license to display the preprint in perpetuity. It is made available under aCC-BY-NC-ND 4.0 International license.

532 substitution of a single base pair (A → G). Then, two independent analyses of them were run
533 using SAW pipeline. The count of mapping reads spatially was shown as the two-dimensional
534 locations and the corresponding mapping number (the tab-delimited file with three columns).
535 Given the cellular size (about 10 μm), these counts were aggregated into bin 20 (20x20
536 DNBs). Bin 20 spots were considered valid only if they had at least 180 reads. The ratio of
537 16S phylotype (A or G) was then calculated, with the frequency histogram shown (**fig. S10**).
538 The dominant phylotypes in bins were defined if the ratio was above 95%. The result was
539 visualized using matplotlib in Python.
540

541 **Phylotype decomposition, phylogenomic analysis of symbiont, and comparison**
542 Pangenome was generated using PanPhlAn version 3.1 (*73*) and in-built scripts of
543 StrainPanDA (*74*). To decompose the diversity of symbiont at the high resolution,
544 StrainPanDA (*74*) was adopted based on the newly constructed pangenome of 30 MAGs and
545 the full set of clean reads. The phylogenetic positions of the two symbiont phylotypes were
546 reconstructed among known chemosynthetic bacteria, utilizing 57 published SOB genomes
547 and the *B. azoricus* MOB symbiont as an outgroup. The phylogenomic analysis was
548 conducted using VEHoP version 1.0 (*75*) to determine their positions at the phylogenomic
549 level. The phylogenomic tree was visualized using tvBOT (*76*). To differentiate between the
550 two symbiont phylotypes, a functional information comparison analysis was performed using
551 METABOLIC□G version 4.0 (*77*), based on the strain decomposition results.
552

553 **Transcriptional profile assembly and quantification**
554 The raw reads were filtered using trimmomatic version 0.39 with the settings
555 (TruSeq3-PE-2.fa:2:30:10:8:true SLIDINGWINDOW:5:20 LEADING:3 TRAILING:3
556 MINLEN:75). Then, qualified reads were mapped to pangenome using Bowtie version 2.3.5
557 (*78*), resulting in the symbiont-derived reads and symbiont-free reads. The symbiotic-free
558 reads were subjected to Trinity version 2.13.2 for de novo assembly (*79*). To prepare for
559 spatial metabarcoding analysis, the host transcripts were first purified using BlobTools
560 version 1.1.1 (*61*) to remove contaminated contigs, and subsequently assessed for coding
561 potential using TransDecoder version 5.7.1 (*80*). Salmon version 1.9.0 (*81*) was performed to
562 quantify the gene expression levels of symbiont.
563

564 **Carbon fixation rate measurements**
565 Radiotracer assays were used to determine the rate of dissolved inorganic carbon (DIC)
566 assimilation by introducing a ^{14}C-labeled DIC tracer to the homogenized gill in sterilizing
567 seawater and quantifying the amount of ^{14}C incorporated into total organic carbon (TOC) (*82*).
568 Gill tissues dissected from fresh samples were homogenized and immediately stored in 20%
569 glycerol in sterile seawater, then slowly thawed on ice prior to downstream analyses. The
570 experimental design details are as follows (**Fig. 5B**): 1) to minimize the impact of varying
571 symbiont numbers on our results, we collected samples from four sites, and four individuals
572 per site; 2) to create a uniform starting point, samples from each site were mixed, and the
573 resulting mixture was divided into sixteen replicates, and these replicates were then assigned
574 to one of four incubation groups at different temperatures (5□, 12□, 20□, and 28□), and

bioRxiv preprint doi: https://doi.org/10.1101/2024.02.25.581922; this version posted April 15, 2025. The copyright holder for this preprint (which was not certified by peer review) is the author/funder, who has granted bioRxiv a license to display the preprint in perpetuity. It is made available under aCC-BY-NC-ND 4.0 International license.

575 incubated in the dark for 46-47 hours; 3) Within each temperature group, we prepared four
576 replicates of gill tissue samples: three experimental samples and one negative control. These
577 samples were placed into 10 ml serum vials, ensuring no headspace, and sealed with sterile
578 PTFE septa and aluminum caps. After that, 100 μL of ^{14}C-DIC solution (~4 × 10^4 Becquerel,
579 Bq) was injected into each serum vial through the stopper by displacing the same volume of
580 water. Before injecting the ^{14}C-DIC tracer, the microorganisms of negative controls were
581 killed by adding 0.5 mL of 100% trichloroacetic acid. Microorganisms of the experimental
582 group were removed with the addition of 0.5 mL and filtered onto 0.2 μm GSWP membranes
583 (polyethersulfone, Millipore) after incubation. The filters were rinsed with 35 ‰ sodium
584 chloride (NaCl) solution (*83*) and transferred into 7 mL scintillation vials containing a 6 mL
585 scintillation cocktail (Ultima Gold ™ Cocktail, PerkinElmer). The radioactivity of the filters
586 was determined using a Tri-Carb 3110TR liquid scintillation counter (*84*). The turnover rate
587 constant (k_n) of DIC was calculated using the equation No. (1), and the assimilation rate
588 (Ass-rate) of DIC was calculated using the equation No. (2):

589 $$k_n = -ln \frac{1-(\frac{DPM-^{14}C-POC}{DPM-14C-DIC})}{t} \quad \mathbf{(1)}$$

590 $$Ass-rate = k_n \times [DIC] \quad \mathbf{(2)}$$

591 k_n: turnover rate constant = day^{-1}.
592 *Ass-rate*: the DIC assimilation rate (μmol·L^{-1}·day^{-1}).
593 *DPM-^{14}C-POC*: the radioactivity on the filter.
594 *DPM-^{14}C-DIC*: the total activity of the added DIC tracer.
595 *t*: the incubation time (day).
596 *[DIC]*: the DIC concentration (mmol·L^{-1}) ranged from 2.019 to 2.229 used in this study.
597

598 **Estimation of the carbon fixation flux of *Thyasira* in the Yellow Sea**

599 We assumed the spatial variation in bottom-layer temperature and thyasirid density in the
600 Yellow Sea to be a result of continuity, though the geological, chemical, and biological
601 processes may also influence this. To avoid over-estimation, the total region for flux
602 estimation was restricted by the maximum region from 139 sampling sites from seven cruises
603 mentioned above (**Fig. 1A**). The bottom water temperature data for this study were derived
604 from the mean annual values for the period 2002-2017 of the World Ocean Atlas 2018 (*85*).
605 Meanwhile, biological distribution data of *Thyasira gouldii* complex (including *T. tokunagai*)
606 were obtained from the Ocean Biodiversity Information System (OBIS; https://obis.org/) and
607 the NBN Atlas (https://nbnatlas.org/). The Python package pykrige.ok version 1.7.2 was
608 employed for the kriging interpolation among sites, predicting the spatial pattern of species
609 density and bottom-layer temperature with a resolution of 0.005 degrees (division unit).
610 The estimation details of total annual carbon fixation flux in the Yellow Sea contributed by
611 this clam are as follows: we measured the DIC assimilation rate at different temperature,
612 while fitted the curve to reconstruct the relationships between turnover rate constant (k_n) and
613 bottom temperature. Based on this relationship, we used the openly available bottom water
614 temperature of the World Ocean Atlas 2018 to predict the turnover rate constant. Then, the
615 DIC assimilation rate was obtained by the DIC concentration multiplied by the turnover rate
616 constant (k_n). Annual carbon fixation flux (Ann-Flux) in each site was calculated using the

bioRxiv preprint doi: https://doi.org/10.1101/2024.02.25.581922; this version posted April 15, 2025. The copyright holder for this preprint (which was not certified by peer review) is the author/funder, who has granted bioRxiv a license to display the preprint in perpetuity. It is made available under aCC-BY-NC-ND 4.0 International license.

617 equation No. (3), mainly incorporating the following parameters: (I) temperature-dependent
618 rate constants (k) from radiocarbon assimilation experiments on *T. tokunagai* (calculated by
619 the equation No. (4); Wilcoxon rank-sum test for site differences at same temperature), (II)
620 interpolated *T. tokunagai* density, (III) interpolated temperature, and (IV) DIC concentration.
621 The total annual carbon fixation flux is the sum of each division unit.

622 $$\boldsymbol{Ann-Flux} = \sum_{n=1}^{area}(\boldsymbol{k_n} \sim \boldsymbol{T_n}) \cdot \boldsymbol{A_n} \cdot [\boldsymbol{DIC}] \cdot \mathbf{12} \cdot \mathbf{365/1000} \quad \textbf{(3)}$$

623 $$\boldsymbol{k_n} = -\mathbf{0.00075756} + \mathbf{0.00033673} * \boldsymbol{T_n} + [-\mathbf{1.698}\boldsymbol{e}^{-05}] * \boldsymbol{T_n}^{2} + \mathbf{2.5}\boldsymbol{e}^{-07} * \boldsymbol{T_n}^{3}$$
624 **(4)**

625 *Ann-Flux*: annual carbon fixation flux (g C · yr^{-1}).
626 $k_n \sim T_n$: the relationship between rate constant and temperature.
627 T_n: the predicted spatial temperature via krige exploitation (□).
628 A_n: the predicted spatial abundance of *Thyasira tokunagai* via krige exploitation
629 (m^2·$individual^{-1}$).
630 *[DIC]*: the concentration ranged from 2.019 and 2.229 (mmol·L^{-1}).
631 12: the molar mass of carbon (g·mol^{-1}).
632 365: assuming the total number of days in a year (day).
633

634 ## Acknowledgments

635 This work was financially supported by the National Natural Science Foundation of China
636 (42476135), Science and Technology Innovation Project of Laoshan Laboratory
637 (LSKJ202203104 and 2022LSL050104-6), the Fundamental Research Funds for the Central
638 Universities (202172002 and 202241002), and the Young Taishan Scholars Program of
639 Shandong Province (tsqn202103036). Data and samples were collected onboard R/V "*Lanhai*
640 *101*" implementing the open research cruises NORC2020-01 and NORC2021-01 supported
641 by the NSFC Ship Time Sharing Project (project numbers: 41949901 and 42049901). We
642 thank Suzanne C. Dufour (Memorial University of Newfoundland) for her constructive
643 comments during the preparation of this paper.

644

645 ## Author contribution

646 JS conceived the project. ML collected the samples, extracted the nucleic acid, and performed
647 most of the experiments and bioinformatic analysis. YL performed the strain decomposition
648 and the carbon fixation estimations. ML and YL drafted the original manuscript. SM
649 estimated the DIC assimilation rate of the symbiont. CC identified the specimens. YL, MS,
650 CC, YL, XL, GCZ, WZ, and JS contributed to the writing and editing of the manuscript.

651

652 ## Data and materials availability

653 The data of this study were deposited in the NCBI database under the BioProject ID
654 PRJNA995037 and PRJNA1016492. All data are available in the main text or the
655 supplementary materials.

bioRxiv preprint doi: https://doi.org/10.1101/2024.02.25.581922; this version posted April 15, 2025. The copyright holder for this preprint (which was not certified by peer review) is the author/funder, who has granted bioRxiv a license to display the preprint in perpetuity. It is made available under aCC-BY-NC-ND 4.0 International license.

656

657 **References**

658 1. M. Hügler, S. M. Sievert, Beyond the Calvin Cycle: Autotrophic Carbon Fixation in
659 the Ocean. *Annu. Rev. Mar. Science* **3**, 261-289 (2011).
660 2. F. Ricci, C. Greening, Chemosynthesis: a neglected foundation of marine ecology and
661 biogeochemistry. *Trends Microbiol.*, (2024).
662 3. J. G. Passos, L. F. Soares, P. Y. G. Sumida, A. G. Bendia, F. M. Nakamura, V. H.
663 Pellizari, C. N. Signori, Contribution of chemoautotrophy and heterotrophy to the
664 microbial carbon cycle in the Southwestern Atlantic Ocean. *Ocean and Coastal*
665 *Research* **70**, e22044 (2023).
666 4. F. Ricci, P. M. Leung, T. Hutchinson, T. Nguyen-Dinh, A. v. S. Hood, V. W. Salazar, V.
667 Eate, W. W. Wong, P. L. M. Cook, C. Greening, H. McClelland, Chemosynthesis
668 enhances carbon fixation in an active microbialite ecosystem. *bioRxiv*,
669 2024.2012.2018.629060 (2025).
670 5. H. T. S. Boschker, D. Vasquez-Cardenas, H. Bolhuis, T. W. C. Moerdijk-Poortvliet, L.
671 Moodley, Chemoautotrophic Carbon Fixation Rates and Active Bacterial
672 Communities in Intertidal Marine Sediments. *PLoS ONE* **9**, e101443 (2014).
673 6. N. Dubilier, C. Bergin, C. Lott, Symbiotic diversity in marine animals: the art of
674 harnessing chemosynthesis. *Nat. Rev. Microbiol.* **6**, 725-740 (2008).
675 7. E. M. Sogin, M. Kleiner, C. Borowski, H. R. Gruber-Vodicka, N. Dubilier, Life in the
676 dark: phylogenetic and physiological diversity of chemosynthetic symbioses. *Annu.*
677 *Rev. Microbiol.* **75**, 695-718 (2021).
678 8. E. M. Sogin, N. Leisch, N. Dubilier, Chemosynthetic symbioses. *Curr. Biol.* **30**,
679 R1137-R1142 (2020).
680 9. Q. Chang, Z. Zhang, Y. Liu, T. Zhang, Carbon fixation by chemoautotrophic microbes
681 and strategies for their artificial regulation. *Chin. Sci. Bull.* **68**, 3792-3808 (2023).
682 10. U. Cardini, M. Bartoli, S. Lücker, M. Mooshammer, J. Polzin, R. W. Lee, V. Micić, T.
683 Hofmann, M. Weber, J. M. Petersen, Chemosymbiotic bivalves contribute to the
684 nitrogen budget of seagrass ecosystems. *ISME J.* **13**, 3131-3134 (2019).
685 11. R. T. Batstone, J. R. Laurich, F. Salvo, S. C. Dufour, Divergent
686 chemosymbiosis-related characters in *Thyasira* cf. *gouldi* (Bivalvia: Thyasiridae).
687 *PLoS ONE* **9**, e92856 (2014).
688 12. I. Killeen, P. G. Oliver, The taxonomic and conservation status of Thyasira gouldi
689 (Philippi, 1844), the northern hatchet shell, in British waters. *Journal of Conchology*
690 **37**, 391-402 (2002).
691 13. Y.-R. Kim, S. Lee, J. Kim, C.-J. Kim, K.-Y. Choi, C.-S. Chung, *Thyasira tokunagai* as
692 an ecological indicator for the quality of sediment and benthic communities in the
693 East Sea-Byeong, Korea. *Mar. Pollut. Bull.* **135**, 873-879 (2018).
694 14. Y. Xu, L. Ma, J. Sui, X. Li, H. Wang, B. Zhang, Potential effects of climate change on
695 the habitat suitability of macrobenthos in the Yellow Sea and East China Sea. *Mar.*
696 *Pollut. Bull.* **174**, 113238 (2022).

bioRxiv preprint doi: https://doi.org/10.1101/2024.02.25.581922; this version posted April 15, 2025. The copyright holder for this preprint (which was not certified by peer review) is the author/funder, who has granted bioRxiv a license to display the preprint in perpetuity. It is made available under aCC-BY-NC-ND 4.0 International license.

697 15. L. Xiao-Shou, N. Da-Peng, Z. xin, Z. Zhi-Nan, Structure of benthic foot web and
698 trophic relationship of macrofauna in the Yellow Sea. *Period. Ocean Univ. China* **50**,
699 20-33 (2020).
700 16. S. C. Dufour, Gill anatomy and the evolution of symbiosis in the bivalve family
701 Thyasiridae. *Biol. Bull.* **208**, 200-212 (2005).
702 17. C. Jain, L. M. Rodriguez-R, A. M. Phillippy, K. T. Konstantinidis, S. Aluru, High
703 throughput ANI analysis of 90K prokaryotic genomes reveals clear species boundaries.
704 *Nat. Commun.* **9**, 5114 (2018).
705 18. B. McCuaig, L. Peña-Castillo, S. C. Dufour, Metagenomic analysis suggests broad
706 metabolic potential in extracellular symbionts of the bivalve *Thyasira* cf. *gouldi*. *Anim.*
707 *Microbiome* **2**, 7 (2020).
708 19. M. Rubin-Blum, N. Dubilier, M. Kleiner, Genetic Evidence for Two Carbon Fixation
709 Pathways (the Calvin-Benson-Bassham Cycle and the Reverse Tricarboxylic Acid
710 Cycle) in Symbiotic and Free-Living Bacteria. *mSphere* **4**, (2019).
711 20. N. Jiao, Y. Liang, Y. Zhang, J. Liu, Y. Zhang, R. Zhang, M. Zhao, M. Dai, W. Zhai, K.
712 Gao, J. Song, D. Yuan, C. Li, G. Lin, X. Huang, H. Yan, L. Hu, Z. Zhang, L. Wang, C.
713 Cao, Y. Luo, T. Luo, N. Wang, H. Dang, D. Wang, S. Zhang, Carbon pools and fluxes
714 in the China Seas and adjacent oceans. *Science China Earth Sciences* **61**, 1535-1563
715 (2018).
716 21. J. Zhang, R. Liu, S. Xi, R. Cai, X. Zhang, C. Sun, A novel bacterial thiosulfate
717 oxidation pathway provides a new clue about the formation of zero-valent sulfur in
718 deep sea. *ISME J.* **14**, 2261-2274 (2020).
719 22. L. H. Gregersen, D. A. Bryant, N.-U. Frigaard, Mechanisms and evolution of
720 oxidative sulfur metabolism in green sulfur bacteria. *Front. Microbiol.* **2**, 116 (2011).
721 23. S. C. Dufour, H. Felbeck, Symbiont abundance in thyasirids (Bivalvia) is related to
722 particulate food and sulphide availability. *Mar. Ecol. Prog. Ser.* **320**, 185-194 (2006).
723 24. B. McCuaig, F. Liboiron, S. C. Dufour, The bivalve Thyasira cf. gouldi hosts
724 chemoautotrophic symbiont populations with strain level diversity. *PeerJ* **5**, e3597
725 (2017).
726 25. K. Anantharaman, M. B. Duhaime, J. A. Breier, K. A. Wendt, B. M. Toner, G. J. Dick,
727 Sulfur Oxidation Genes in Diverse Deep-Sea Viruses. *Science* **344**, 757-760 (2014).
728 26. J. M. Klatt, L. Polerecky, Assessment of the stoichiometry and efficiency of CO2
729 fixation coupled to reduced sulfur oxidation. *Front. Microbiol.* **6**, 484 (2015).
730 27. G. F. Paredes, T. Viehboeck, R. Lee, M. Palatinszky, M. A. Mausz, S. Reipert, A.
731 Schintlmeister, A. Maier, J.-M. Volland, C. Hirschfeld, Anaerobic sulfur oxidation
732 underlies adaptation of a chemosynthetic symbiont to oxic-anoxic interfaces.
733 *Msystems* **6**, 10.1128/msystems. 01186-01120 (2021).
734 28. T. J. Hackmann, Setting new boundaries of 16S rRNA gene identity for prokaryotic
735 taxonomy. *Int. J. Syst. Evol. Microbiol.* **75**, (2025).
736 29. R. Ansorge, S. Romano, L. Sayavedra, M. Á. G. Porras, A. Kupczok, H. E.
737 Tegetmeyer, N. Dubilier, J. Petersen, Functional diversity enables multiple symbiont
738 strains to coexist in deep-sea mussels. *Nat. Microbiol.* **4**, 2487-2497 (2019).

bioRxiv preprint doi: https://doi.org/10.1101/2024.02.25.581922; this version posted April 15, 2025. The copyright holder for this preprint (which was not certified by peer review) is the author/funder, who has granted bioRxiv a license to display the preprint in perpetuity. It is made available under aCC-BY-NC-ND 4.0 International license.

739 30. S. C. Dufour, H. Felbeck, Sulphide mining by the superextensile foot of symbiotic
740 thyasirid bivalves. *Nature* **426**, 65-67 (2003).
741 31. S. C. Dufour, J. R. Laurich, R. T. Batstone, B. McCuaig, A. Elliott, K. M. Poduska,
742 Magnetosome-containing bacteria living as symbionts of bivalves. *ISME J.* **8**,
743 2453-2462 (2014).
744 32. J. E. Hansen, P. Kharecha, M. Sato, G. Tselioudis, J. Kelly, S. E. Bauer, R. Ruedy, E.
745 Jeong, Q. Jin, E. Rignot, Global Warming Has Accelerated: Are the United Nations
746 and the Public Well-Informed? *Environ.: Sci. Policy Sustainable Dev.* **67**, 6-44 (2025).
747 33. T. R. Karl, K. E. Trenberth, Modern global climate change. *science* **302**, 1719-1723
748 (2003).
749 34. F. Wang, J. Liu, G. Qin, J. Zhang, J. Zhou, J. Wu, L. Zhang, P. Thapa, C. J. Sanders, I.
750 R. Santos, X. Li, G. Lin, Q. Weng, J. Tang, N. Jiao, H. Ren, Coastal blue carbon in
751 China as a nature-based solution toward carbon neutrality. *The Innovation* **4**, (2023).
752 35. A. Braun, M. Spona-Friedl, M. Avramov, M. Elsner, F. Baltar, T. Reinthaler, G. J.
753 Herndl, C. Griebler, Reviews and syntheses: Heterotrophic fixation of inorganic
754 carbon-significant but invisible flux in environmental carbon cycling. *Biogeosciences*
755 **18**, 3689-3700 (2021).
756 36. F. Baltar, G. J. Herndl, Ideas and perspectives: Is dark carbon fixation relevant for
757 oceanic primary production estimates? *Biogeosciences* **16**, 3793-3799 (2019).
758 37. D. J. Amaya, M. G. Jacox, M. A. Alexander, J. D. Scott, C. Deser, A. Capotondi, A. S.
759 Phillips, Bottom marine heatwaves along the continental shelves of North America.
760 *Nat. Commun.* **14**, 1038 (2023).
761 38. V. V. Menezes, A. M. Macdonald, C. Schatzman, Accelerated freshening of Antarctic
762 Bottom Water over the last decade in the Southern Indian Ocean. *Sci. Adv.* **3**,
763 e1601426 (2017).
764 39. G. C. Johnson, A. S. Mahmud, A. M. Macdonald, B. S. Twining, Antarctic bottom
765 water warming, freshening, and contraction in the eastern Bellingshausen Basin.
766 *Geophys. Res. Lett.* **51**, e2024GL109937 (2024).
767 40. P. Yang, B. Sun, Y. Zhang, Changing circulations challenge the sustainability of cold
768 water mass and associated ecosystem under climate change. *npj Ocean Sustainability*
769 **3**, 42 (2024).
770 41. T. Xu, Y. Sun, Z. Wang, A. Sen, P.-Y. Qian, J.-W. Qiu, The Morphology, Mitogenome,
771 Phylogenetic Position, and Symbiotic Bacteria of a New Species of Sclerolinum
772 (Annelida: Siboglinidae) in the South China Sea. *Front. Mar. Sci.* **8**, (2022).
773 42. W. Bernhard, A new staining procedure for electron microscopical cytology. *J.*
774 *Ultrastruct. Res.* **27**, 250-265 (1969).
775 43. H. Daims, A. Brühl, R. Amann, K.-H. Schleifer, M. Wagner, The domain-specific
776 probe EUB338 is insufficient for the detection of all bacteria: development and
777 evaluation of a more comprehensive probe set. *Syst. Appl. Microbiol.* **22**, 434-444
778 (1999).
779 44. J. Ye, G. Coulouris, I. Zaretskaya, I. Cutcutache, S. Rozen, T. L. Madden,
780 Primer-BLAST: A tool to design target-specific primers for polymerase chain reaction.
781 *BMC Bioinf.* **13**, 134 (2012).

bioRxiv preprint doi: https://doi.org/10.1101/2024.02.25.581922; this version posted April 15, 2025. The copyright holder for this preprint (which was not certified by peer review) is the author/funder, who has granted bioRxiv a license to display the preprint in perpetuity. It is made available under aCC-BY-NC-ND 4.0 International license.

782 45. A. Bahobail, S. G. El-Rab, G. Amin, Locally isolated bacterial strains with multiple
783 degradation potential capabilities on petroleum hydrocarbon pollutants. *Advances in*
784 *Microbiology* **6**, 852-866 (2016).
785 46. J. G. Caporaso, J. Kuczynski, J. Stombaugh, K. Bittinger, F. D. Bushman, E. K.
786 Costello, N. Fierer, A. G. Peña, J. K. Goodrich, J. I. Gordon, G. A. Huttley, S. T.
787 Kelley, D. Knights, J. E. Koenig, R. E. Ley, C. A. Lozupone, D. McDonald, B. D.
788 Muegge, M. Pirrung, J. Reeder, J. R. Sevinsky, P. J. Turnbaugh, W. A. Walters, J.
789 Widmann, T. Yatsunenko, J. Zaneveld, R. Knight, QIIME allows analysis of
790 high-throughput community sequencing data. *Nat. Methods* **7**, 335-336 (2010).
791 47. R. R. Wick, L. M. Judd, K. E. Holt, Performance of neural network basecalling tools
792 for Oxford Nanopore sequencing. *Genome Biol.* **20**, 129 (2019).
793 48. A. M. Bolger, M. Lohse, B. Usadel, Trimmomatic: a flexible trimmer for Illumina
794 sequence data. *Bioinformatics* **30**, 2114-2120 (2014).
795 49. N. Dierckxsens, P. Mardulyn, G. Smits, NOVOPlasty: de novo assembly of organelle
796 genomes from whole genome data. *Nucleic Acids Res.* **45**, e18-e18 (2016).
797 50. M. Bernt, A. Donath, F. Jühling, F. Externbrink, C. Florentz, G. Fritzsch, J. Pütz, M.
798 Middendorf, P. F. Stadler, MITOS: improved de novo metazoan mitochondrial
799 genome annotation. *Mol. Phylogenet. Evol.* **69**, 313-319 (2013).
800 51. R. C. Edgar, MUSCLE: multiple sequence alignment with high accuracy and high
801 throughput. *Nucleic Acids Res.* **32**, 1792-1797 (2004).
802 52. J. Castresana, Selection of Conserved Blocks from Multiple Alignments for Their Use
803 in Phylogenetic Analysis. *Mol. Biol. Evol.* **17**, 540-552 (2000).
804 53. S. Kumar, G. Stecher, M. Li, C. Knyaz, K. Tamura, MEGA X: molecular evolutionary
805 genetics analysis across computing platforms. *Mol. Biol. Evol.* **35**, 1547-1549 (2018).
806 54. J. Rozas, A. Ferrer-Mata, J. C. Sánchez-DelBarrio, S. Guirao-Rico, P. Librado, S. E.
807 Ramos-Onsins, A. Sánchez-Gracia, DnaSP 6: DNA sequence polymorphism analysis
808 of large data sets. *Mol. Biol. Evol.* **34**, 3299-3302 (2017).
809 55. J. W. Leigh, D. Bryant, Popart: full-feature software for haplotype network
810 construction. *Methods Ecol. Evol.* **6**, 1110-1116 (2015).
811 56. K. Katoh, K. Misawa, K. i. Kuma, T. Miyata, MAFFT: a novel method for rapid
812 multiple sequence alignment based on fast fourier transform. *Nucleic Acids Res.* **30**,
813 3059-3066 (2002).
814 57. D. Falush, M. Stephens, J. K. Pritchard, Inference of population structure using
815 multilocus genotype data: linked loci and correlated allele frequencies. *Genetics* **164**,
816 1567-1587 (2003).
817 58. D. A. Earl, B. M. vonHoldt, STRUCTURE HARVESTER: a website and program for
818 visualizing STRUCTURE output and implementing the Evanno method. *Conserv.*
819 *Genet. Resour.* **4**, 359-361 (2012).
820 59. D. Li, C.-M. Liu, R. Luo, K. Sadakane, T.-W. Lam, MEGAHIT: an ultra-fast
821 single-node solution for large and complex metagenomics assembly via succinct de
822 Bruijn graph. *Bioinformatics* **31**, 1674-1676 (2015).

bioRxiv preprint doi: https://doi.org/10.1101/2024.02.25.581922; this version posted April 15, 2025. The copyright holder for this preprint (which was not certified by peer review) is the author/funder, who has granted bioRxiv a license to display the preprint in perpetuity. It is made available under aCC-BY-NC-ND 4.0 International license.

823 60. Y.-W. Wu, B. A. Simmons, S. W. Singer, MaxBin 2.0: an automated binning algorithm
824 to recover genomes from multiple metagenomic datasets. *Bioinformatics* **32**, 605-607
825 (2015).
826 61. D. Laetsch, M. Blaxter, BlobTools: Interrogation of genome assemblies.
827 *F1000Research* **6**, (2017).
828 62. J. Hu, Z. Wang, Z. Sun, B. Hu, A. O. Ayoola, F. Liang, J. Li, J. R. Sandoval, D. N.
829 Cooper, K. Ye, J. Ruan, C.-L. Xiao, D. Wang, D.-D. Wu, S. Wang, NextDenovo: an
830 efficient error correction and accurate assembly tool for noisy long reads. *Genome*
831 *Biol.* **25**, 107 (2024).
832 63. J. Hu, Z. Wang, Z. Sun, B. Hu, A. O. Ayoola, F. Liang, J. Li, J. R. Sandoval, D. N.
833 Cooper, K. Ye, J. Ruan, C.-L. Xiao, D.-P. Wang, D.-D. Wu, S. Wang, An efficient
834 error correction and accurate assembly tool for noisy long reads. *bioRxiv*, 531669
835 (2023).
836 64. J. Hu, J. Fan, Z. Sun, S. Liu, NextPolish: a fast and efficient genome polishing tool for
837 long-read assembly. *Bioinformatics* **36**, 2253-2255 (2019).
838 65. A. Chklovski, D. H. Parks, B. J. Woodcroft, G. W. Tyson, CheckM2: a rapid, scalable
839 and accurate tool for assessing microbial genome quality using machine learning. *Nat.*
840 *Methods* **20**, 1203-1212 (2023).
841 66. P.-A. Chaumeil, A. J. Mussig, P. Hugenholtz, D. H. Parks, GTDB-Tk v2: memory
842 friendly classification with the genome taxonomy database. *Bioinformatics* **38**,
843 5315-5316 (2022).
844 67. T. Seemann, Prokka: rapid prokaryotic genome annotation. *Bioinformatics* **30**,
845 2068-2069 (2014).
846 68. B. Buchfink, C. Xie, D. H. Huson, Fast and sensitive protein alignment using
847 DIAMOND. *Nat. Methods* **12**, 59-60 (2015).
848 69. A. Conesa, S. Götz, J. M. García-Gómez, J. Terol, M. Talón, M. Robles, Blast2GO: a
849 universal tool for annotation, visualization and analysis in functional genomics
850 research. *Bioinformatics* **21**, 3674-3676 (2005).
851 70. M. Y. Galperin, Y. I. Wolf, K. S. Makarova, R. Vera Alvarez, D. Landsman, E. V.
852 Koonin, COG database update: focus on microbial diversity, model organisms, and
853 widespread pathogens. *Nucleic Acids Res.* **49**, D274-D281 (2020).
854 71. M. Kanehisa, Y. Sato, K. Morishima, BlastKOALA and GhostKOALA: KEGG tools
855 for functional characterization of genome and metagenome sequences. *J. Mol. Biol.*
856 **428**, 726-731 (2016).
857 72. A. Chen, S. Liao, M. Cheng, K. Ma, L. Wu, Y. Lai, X. Qiu, J. Yang, J. Xu, S. Hao,
858 Spatiotemporal transcriptomic atlas of mouse organogenesis using DNA
859 nanoball-patterned arrays. *Cell* **185**, 1777-1792. e1721 (2022).
860 73. F. Beghini, L. J. McIver, A. Blanco-Míguez, L. Dubois, F. Asnicar, S. Maharjan, A.
861 Mailyan, P. Manghi, M. Scholz, A. M. Thomas, M. Valles-Colomer, G. Weingart, Y.
862 Zhang, M. Zolfo, C. Huttenhower, E. A. Franzosa, N. Segata, Integrating taxonomic,
863 functional, and strain-level profiling of diverse microbial communities with
864 bioBakery 3. *eLife* **10**, e65088 (2021).

bioRxiv preprint doi: https://doi.org/10.1101/2024.02.25.581922; this version posted April 15, 2025. The copyright holder for this preprint (which was not certified by peer review) is the author/funder, who has granted bioRxiv a license to display the preprint in perpetuity. It is made available under aCC-BY-NC-ND 4.0 International license.

865 74. H. Hu, Y. Tan, C. Li, J. Chen, Y. Kou, Z. Z. Xu, Y. Y. Liu, Y. Tan, L. Dai,
866 StrainPanDA: Linked reconstruction of strain composition and gene content profiles
867 via pangenome‐based decomposition of metagenomic data. *iMeta* **1**, e41 (2022).
868 75. Y. Li, X. Liu, C. Chen, J.-W. Qiu, K. Kocot, J. Sun, VEHoP: A Versatile, Easy-to-use,
869 and Homology-based Phylogenomic pipeline accommodating diverse sequences.
870 *bioRxiv*, (2024).
871 76. J. Xie, Y. Chen, G. Cai, R. Cai, Z. Hu, H. Wang, Tree Visualization By One Table
872 (tvBOT): a web application for visualizing, modifying and annotating phylogenetic
873 trees. *Nucleic Acids Res.* **51**, W587-W592 (2023).
874 77. Z. Zhou, P. Q. Tran, A. M. Breister, Y. Liu, K. Kieft, E. S. Cowley, U. Karaoz, K.
875 Anantharaman, METABOLIC: high-throughput profiling of microbial genomes for
876 functional traits, metabolism, biogeochemistry, and community-scale functional
877 networks. *Microbiome* **10**, 33 (2022).
878 78. B. Langmead, S. L. Salzberg, Fast gapped-read alignment with Bowtie 2. *Nat.*
879 *Methods* **9**, 357-359 (2012).
880 79. M. G. Grabherr, B. J. Haas, M. Yassour, J. Z. Levin, D. A. Thompson, I. Amit, X.
881 Adiconis, L. Fan, R. Raychowdhury, Q. Zeng, Full-length transcriptome assembly
882 from RNA-Seq data without a reference genome. *Nat. Biotechnol.* **29**, 644-652
883 (2011).
884 80. B. Haas, A. Papanicolaou, TransDecoder (find coding regions within transcripts).
885 *Google Scholar*, (2016).
886 81. R. Patro, G. Duggal, M. I. Love, R. A. Irizarry, C. Kingsford, Salmon provides fast
887 and bias-aware quantification of transcript expression. *Nat. Methods* **14**, 417-419
888 (2017).
889 82. G.-C. Zhuang, A. Montgomery, S. B. Joye, Heterotrophic metabolism of C1 and C2
890 low molecular weight compounds in northern Gulf of Mexico sediments: controlling
891 factors and implications for organic carbon degradation. *Geochim. Cosmochim. Acta*
892 **247**, 243-260 (2019).
893 83. G. C. Zhuang, T. D. Peña‐Montenegro, A. Montgomery, J. P. Montoya, S. B. Joye,
894 Significance of acetate as a microbial carbon and energy source in the water column
895 of Gulf of Mexico: implications for marine carbon cycling. *Global Biogeochem.*
896 *Cycles* **33**, 223-235 (2019).
897 84. S.-H. Mao, H.-H. Zhang, G.-C. Zhuang, X.-J. Li, Q. Liu, Z. Zhou, W.-L. Wang, C.-Y.
898 Li, K.-Y. Lu, X.-T. Liu, Aerobic oxidation of methane significantly reduces global
899 diffusive methane emissions from shallow marine waters. *Nat. Commun.* **13**, 7309
900 (2022).
901 85. M. Locarnini, A. Mishonov, O. Baranova, T. Boyer, M. Zweng, H. Garcia, D. Seidov,
902 K. Weathers, C. Paver, I. Smolyar, World ocean atlas 2018, volume 1: Temperature.
903 (2018).

bioRxiv preprint doi: https://doi.org/10.1101/2024.02.25.581922; this version posted April 15, 2025. The copyright holder for this preprint (which was not certified by peer review) is the author/funder, who has granted bioRxiv a license to display the preprint in perpetuity. It is made available under aCC-BY-NC-ND 4.0 International license.

904 **Figure legends**

905 **Fig. 1 Sampling sites, stable isotope signatures, and chemosymbionts. (A)** Shell and
906 external anatomy of *T. tokunagai*, and a total of 139 sampling sites during seven research
907 cruises from 2018-2024 in the Yellow Sea. Abbreviation: g, gill; f, foot; d, digestive
908 diverticula; m, mantle; aa, anterior adductor; pa: posterior adductor. **(B)** The stable isotopic
909 niche of *T. tokunagai* in the macrobenthic community of the Yellow Sea. Additional data on
910 other macrobenthos in the Yellow Sea can be found in Table S2 (*15*). The red dots represent *T.*
911 *tokunagai.* **(C)** Transmission electron microscopy (TEM) image of extracellular bacteria
912 maintained in pouch-like structure bearing microvilli. Abbreviation: mv, microvilli; b,
913 bacteria (the high abundance bacteria are mainly symbiont); n, nuclei; m, cell membrane; c,
914 cell cytoplasm; h, hemocoel. **(D)** Fluorescence *in situ* hybridization (FISH) showing the
915 symbiont bacteria in the gill filaments. All cell nuclei were stained with DAPI, the cell
916 membrane was stained by concanavalin-A, and symbionts were hybridized by the specific
917 probe of the *T. tokunagai* symbiont *Sedimenticola* sp.

918 **Fig. 2. Identification and spatial distribution of the two *Sedimenticola* symbiont**
919 **phylotypes in *Thyasira tokunagai* gill tissue. (A)** Two dominant phylotypes belonging to
920 the genus *Sedimenticola* were identified in gill tissue bacterial communities which we call
921 *Sedimenticola* sp. (ex *Thyasira tokunagai*) 'phylotype A' and 'phylotype G' based on 16S
922 rRNA gene sequencing, differing by a single base at the 563rd position; the first 13 samples
923 were used for metagenomic sequencing, while the last 8 were used for metatranscriptomic
924 sequencing. NYS represents the sampling sites from the north Yellow Sea, whereas SYS
925 represents the sampling sites from the south Yellow Sea. **(B)** Strain decomposition analysis
926 revealed the presence of two symbiont phylotype, corresponding to the two dominant
927 phylotypes identified in (A). **(C)** The H&E-stained gill tissue section (scale bar: 1 mm) had a
928 neighboring section used for spatial phylotype distribution analysis (see panel E). **(D)** FISH
929 imaging showing the symbiont-specific probe visualized spatial distribution in a gill tissue
930 section (scale bar: 1 mm), while a neighboring section was observed after hematoxylin and
931 eosin (H&E) staining (see panel C and E). **(E)** At the cellular level, the spatial distribution of
932 symbiont phylotypes is such that each spot represents a 10 μm bin, named bin 20,
933 approximating the size of a single cell, and the A/G ratio indicates the relative abundance of
934 phylotype A compared to phylotype G at each location (e.g., A/G > 19 indicates that
935 phylotype A is approximately 19 times more abundant than phylotype G within that bin).

936 **Fig. 3. Phylogenetic relationships of the two *Sedimenticola* symbiont phylotypes. (A)**
937 General features of the symbiont genomes showing that the two genomes have a similar size
938 (a total of 4.5 Mb) and a GC content of 52.19%. **(B)** Phylogenomic analysis, rooted with the
939 methanotrophic (MOB) symbiont of the hot vent bathymodioline mussel *Bathymodiolus*
940 *azoricus,* demonstrates that the two phylotypes fall within the family Sedimenticolaceae
941 (SOB) and are closely related to cultured *Sedimenticola* species (solid black dot at the node
942 indicates 100 bootstrap supports; scale bar: 0.1 substitutions per nucleotide site).

943

bioRxiv preprint doi: https://doi.org/10.1101/2024.02.25.581922; this version posted April 15, 2025. The copyright holder for this preprint (which was not certified by peer review) is the author/funder, who has granted bioRxiv a license to display the preprint in perpetuity. It is made available under aCC-BY-NC-ND 4.0 International license.

Fig. 4. Chemosynthetic capacities and transcriptome profiles of symbiont phylotypes. (A) Reconstructed chemosynthesis pathways from both symbiont genomes indicate a conserved metabolic potential, consistent with a free-living lifestyle. Both phylotypes encode a complete set of enzymes for carbon fixation and utilization and have the potential to utilize sulfides and hydrogen as energy sources. **(B)** Transcriptome profiles of highly conserved chemosynthetic pathways related to carbon, sulfur, nitrogen, and hydrogen metabolism. Transcribed functional genes were annotated against the KEGG database, and expression levels are shown as log2-normalized Transcripts Per Kilobase Million (TPM).

Fig. 5 Global distribution of the *Thyasira gouldii* complex and the carbon fixation rate of *T. tokunagai.* **(A)** Global distribution of the *Thyasira gouldii* complex, and *Thyasira tokunagai* distributed in the Yellow Sea and Japan Sea. **(B)** Flow of the ^{14}C-labeled DIC assimilation assay. To assess DIC assimilation, gill tissue samples were dissected, homogenized in sterilized seawater, and aliquoted into sealed penicillin bottles. ^{14}C-labeled DIC tracer was then added, and the samples were incubated for nearly two days at various temperatures (5, 12, 20, and 28 □) before measuring carbon assimilation rates. The symbol of "X" represents the negative control treated by trichloroacetic acid. **(C)** Carbon fixation rate constants at different temperatures (5°C, 12°C, 20°C, 28°C) fitted using a trinomial equation.

Fig. 6 Estimation of the total carbon fixation flux of *Thyasira tokunagai* in Yellow Sea. (A) Visualization of the mean annual bottom water temperature from 2002-2017, and this data was used to predict carbon fixation rate constants. **(B)** *T. tokunagai* density in the Yellow Sea. Based on data from 139 sites across seven cruises, we predicted density using the kriging interpolation method within the sampling area for carbon fixation flux estimation. **(C)** Annual carbon fixation flux within the sampling area is estimated using the kriging interpolation method, units represent the total annual fixed carbon per site.

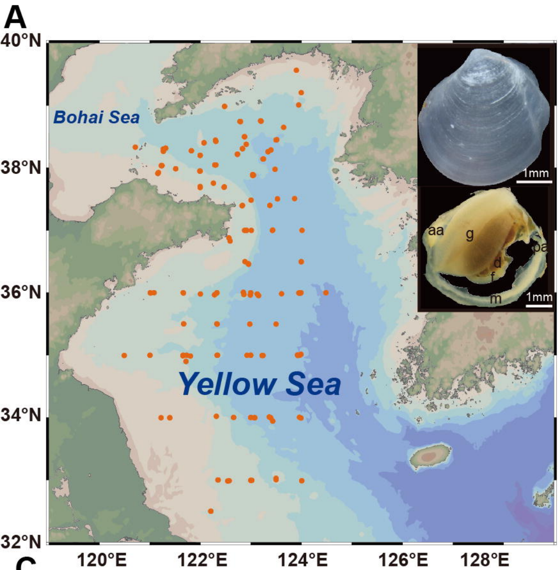
A
Bohai Sea
Yellow Sea
40°N
38°N
36°N
34°N
32°N
120°E
122°E
124°E
126°E
128°E
2000m
1000m
500m
200m
100m
50m
5m
5m
20m
40m
60m
80m
100m
200m
300m
1mm
aa
g
d
f
m
pa

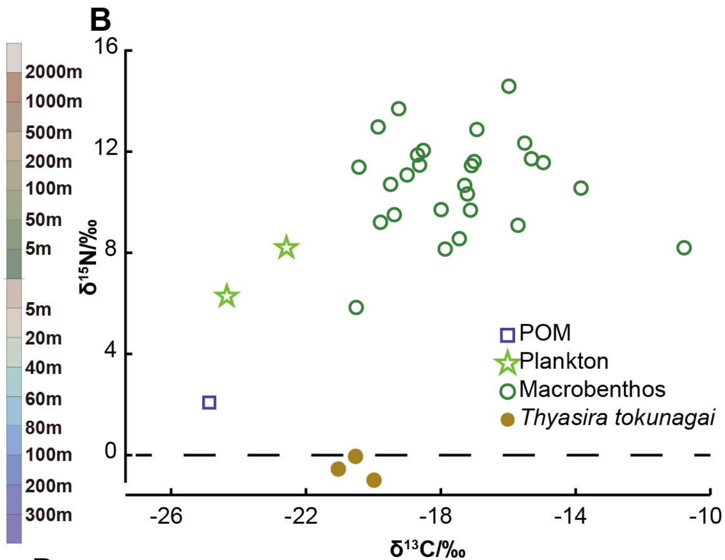
B
δ15N/‰
δ13C/‰
POM
Plankton
Macrobenthos
Thyasira tokunagai

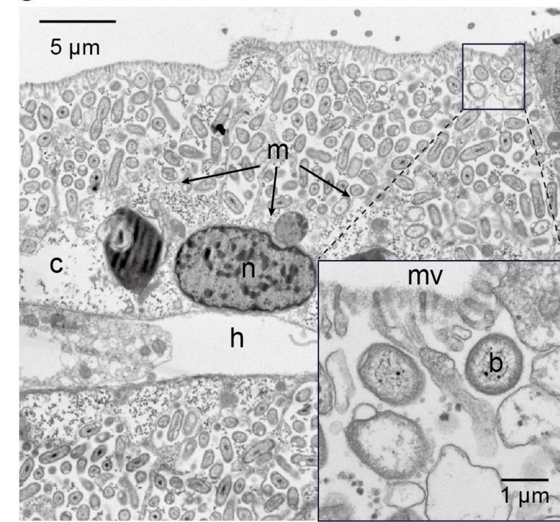
C
5 μm
m
c
n
h
mv
b
1 μm

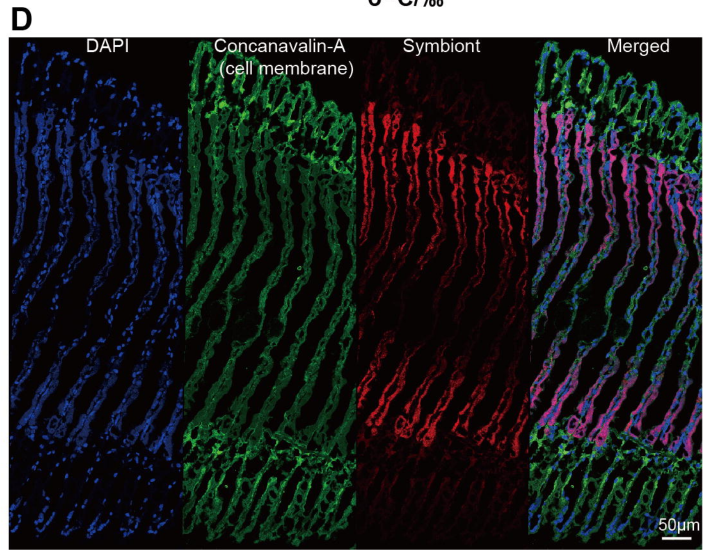
D
DAPI
Concanavalin-A
(cell membrane)
Symbiont
Merged
50μm

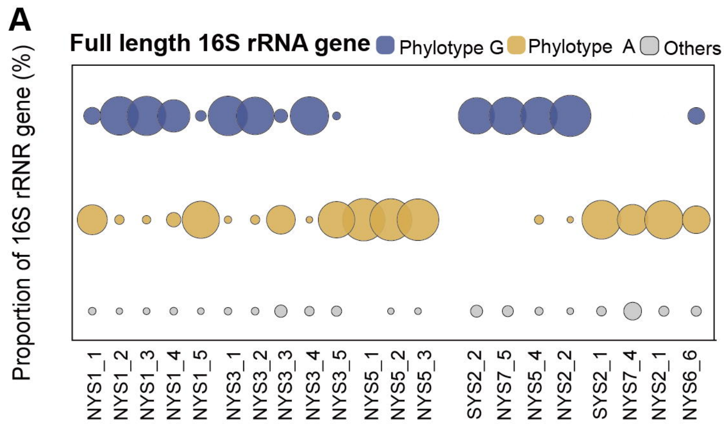

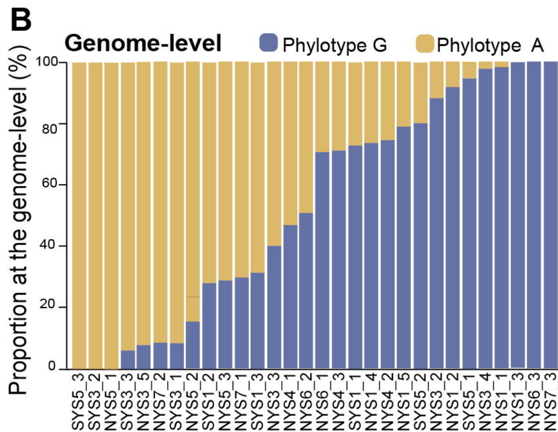

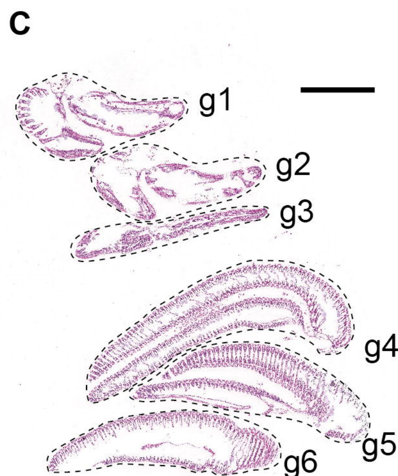

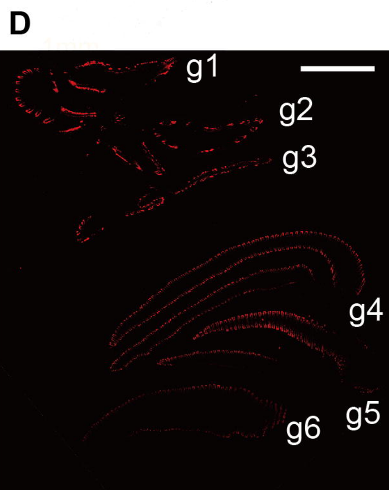

E

Percentage of bin20 (%)

100
75
50
25
0

g1 g2 g3 g4 g5 g6

A/G ≥ 19
G/A ≥ 19
Others

g1
g2
g3
g4
g5
g6

1600
1400
1200
1000
800

Spatial 2

Spatial 1 800 1000 1200 1400

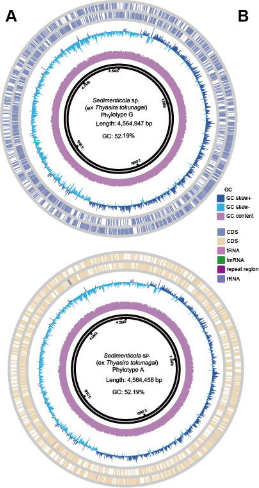
A
Sedimenticola sp.
(ex Thyasira tokunagai)
Phylotype G
Length: 4,564,947 bp
GC: 52.19%
GC
GC skew+
GC skew-
GC content
CDS
CDS
tRNA
tmRNA
repeat region
rRNA
Sedimenticola sp.
(ex Thyasira tokunagai)
Phylotype A
Length: 4,564,458 bp
GC: 52.19%
B
Bathymodiolus azoricus MOB
Bathymodiolus septemdierum SOB
Conchocele bisecta SOB
Bathymodiolus puteoserpentis SOB
Bathymodiolus heckerae SOB
Bathymodiolus thermophilus SOB
Bathymodiolus brooksi SOB
Thilglobaceae
Pliocardiine symbiont clade 1
Thyasira sp. Haima SOB
Pliocardiine symbiont clade 2
0.1
Solemya pervernicosa SOB
Solemya velum SOB
Solemya elarraichensis SOB
Ifremeria nautilei SOB
Sedimenticolaceae
Kuphus polythalamia SOB
Alviniconcha adamantis SOB
Chrysomallon squamiferum SOB
Alviniconcha strummeri SOB
Sedimenticola thiotaurini 3
Phacoides pectinatus SOB
Solemya velesiana SOB
Sedimenticola sp. (ex Thyasira tokunagai) Phylotype G
Sedimenticola sp. (ex Thyasira tokunagai) Phylotype A
Sedimenticola thiotaurini 2
Sedimenticola selenatireducens 2
Sedimenticola
Sedimenticola thiotaurini 1
Sedimenticola selenatireducens DSM17994
Sedimenticola selenatireducens 2
Siboglinid tubeworms symbiont clade 1
Siboglinid tubeworms symbiont clade 2
Lucinidae SOB

A

Nitrogen
NosZ
napA napB
narGHI
Nitrate
Nitrite
NirS
Nitric oxide
norB
norC
Nitrous oxide
NO_2^-
NO_3^-
nrt
Nitrogen metabolism
Biomass (Organic compounds)
CO_2
CBB Cycle
Sulfate
soxA soxB
soxX soxY soxZ
Thiosulfate
phsA
psrA
PPi
Sat
ATP
APS
aprA
aprB
Sulfite
dsrA
dsrB
Sulfide
fccA
fccB
Sulfur
sqr
$(Sulfide)_n$
hydB
$(Sulfide)_{n-1}$
Sulfur metabolism
SO_4^{2-}
$S_2O_3^{2-}$
cysZ
Transporter Heme
Transporter Molybdate
Biosynthesis of amnio acid, vitamins and cofactors
T1SS
Chemotaxis Proteins
Flagellum
Transporter Iron and Znic
hupL
H_2
hyaA
2H+
Glycolysis
acetyl-CoA
TCA Cycle
T6SS
Transporter Phospholipid
hoxU
hoxF
hoxH
hoxY
Transporter Lipoprotein
Inner membrane
Hydrogen metabolism
Transporter Lipopolyaccharide
Outer membrane
Uptake
hupU
hupv
Transporter Phosphate
Transporter Branch-chain amino acid
Pts IHPN
Transporter Microcin C
che
H_2
Sugar

B

glk pgm pgi pfk fbaA tpiA gapA pgk gpml eno pyk aceE aceF lpd gltA acnA icd sucA sucB lpd korA korB sucD sucC sdhA sdhB sdhC sdhD fumA mdh rbcL pgk gapA fbaB fbaA tktA rpiA prkB tpiA rpe sat aprA aprB dsrA dsrB soxA soxX soxY soxZ soxB sqr fccA fccB dsrE dsrF dsrH dsrC amt narK narG narH narI napA napB nirS norB norC nosZ glnA gltB gltD hyaB hyaA hupV hupU hupH hoxF hoxU hoxY

NYS7_5
SYS2_2
NYS6_6
NYS7_4
NYS2_1
NYS2_2
NYS5_4
SYS2_1

12.00
10.00
8.00
6.00
4.00
2.00
0.00
log_2TPM

Glycolysis
TCA cycle
CBB cycle
Sulfur metabolism
Nitrogen metabolism
Hydrogen metabolism

A
20°N
40°N
60°N
80°N
90°E
0
180°W
90°W
Europe
Asia
North America
North Atlantic Ocean
Arctic Ocean
North Pacific Ocean
45°N
40°N
35°N
30°N
115°E
120°E
125°E
130°E
135°E
140°E
145°E
Japan Sea
Pacific Ocean
Yellow Sea
C
DIC assimilation rate constant k
0.00000
0.00256
0.00512
5
12
20
28
Incubate temperature/°C
y ~ x^3; Adj R^2 = 0.52 F = 17.83 P = 1.02e−07
SYS1
SYS2
SYS3
SYS4
B
Dissect
Homogenate
Subpackage
Sterilized seawater
Add ^{14}C-DIC tracer
Incubate
5°C
12°C
20°C
28°C

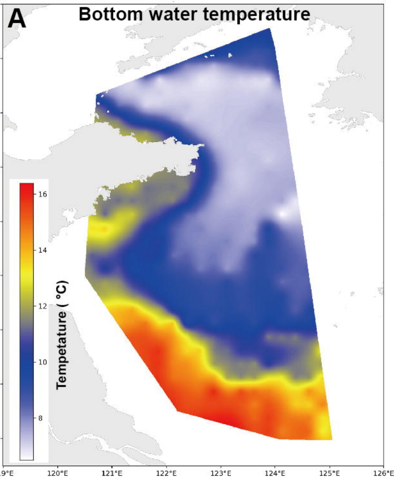
A
Bottom water temperature
Tempetature (°C)
16
14
12
10
8
40°N
39°N
38°N
37°N
36°N
35°N
34°N
33°N
32°N
119°E
120°E
121°E
122°E
123°E
124°E
125°E
126°E

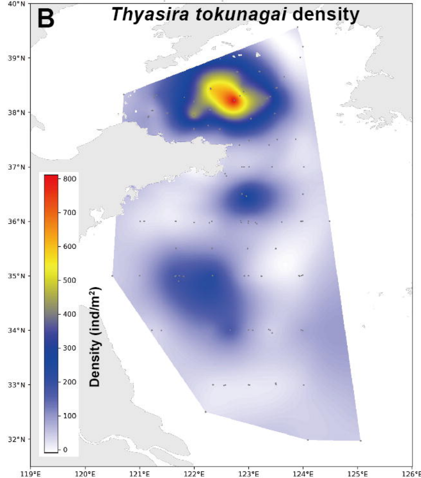
B
Thyasira tokunagai density
Density (ind/m²)
800
700
600
500
400
300
200
100
0
40°N
39°N
38°N
37°N
36°N
35°N
34°N
33°N
32°N
119°E
120°E
121°E
122°E
123°E
124°E
125°E
126°E

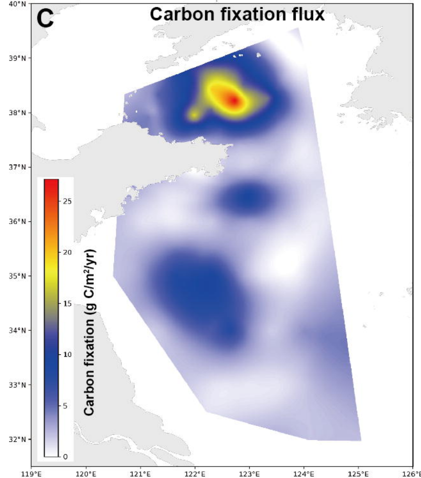
C
Carbon fixation flux
Carbon fixation (g C/m²/yr)
25
20
15
10
5
0
40°N
39°N
38°N
37°N
36°N
35°N
34°N
33°N
32°N
119°E
120°E
121°E
122°E
123°E
124°E
125°E
126°E